



OPEN Study on the synergistic hydration mechanism of granulated blast furnace slag-carbide slag-based cementitious materials and the properties of full-solid waste backfill materials

Jianmin Li¹, Liwen Guo^{1,2,3}✉, Jiayong Zhang^{2,3}✉, Ye Li^{2,3}, Li Ma⁴ & Kai Wang⁵

The synergistic utilization of multiple solid waste is an effective means of achieving green filling and resource utilization of solid waste in mines. In this paper, the synergistic effects of solid waste granulated blast furnace slag (GS) and carbide slag (CS) as cementitious materials (GCCM) are investigated, along with their preliminary feasibility in combination with coal gangue (CG) and furnace bottom slag (FBS) for the preparation of backfill materials. The synergistic hydration mechanism, mechanical properties, working performance of GCCM and GBC were studied, and the environmental impact and cost-effectiveness of GBC were evaluated. The results indicate that when the molar ratio of $n(\text{CaO})/n(\text{SiO}_2 + \text{Al}_2\text{O}_3)$ is 0.635 in GCCM, CS has a significant alkaline excitation effect on GS. In addition, the hydration products mainly composed of C-(A)-S-H gel, AFm and hydrotoalcite. However, when the concentration of OH⁻ is high in GCCM, Ca(OH)₂ preferentially precipitates, leading to a reduction in the amount of main hydration product C-(A)-S-H gel. Moreover, GBC has better competitive strength performance than ordinary Portland cement (OPC). The optimal compressive strength of GBC at 28 days is 19.699 MPa, with a standard slump is 228 mm, fully meeting the strength and transportation requirements for mine filling. The heavy metal leaching rate at 28 days meets the requirements of GB 8978, demonstrating potential for carbon reduction and cost savings. The full-solid waste GBC developed in this study can replace cement as a backfill material, which is of significant importance for achieving green mining, the synergistic utilization of solid waste resources, reducing filling costs, and enhancing environmental benefits.

Keywords Binary solid waste cementitious material, Carbide slag, Synergistic hydration mechanism, Mechanical properties, Full-solid waste backfill materials

According to the data of the Annual Report on the Development of the Coal Industry in 2023, the raw coal production of China is expected to reach 4.71 billion tons by 2023, while coal consumption will grow by 5.6%. Furthermore, the available coal resources are projected to exceed 13.79 billion tons¹. Due to the large thickness of the overburden and the complex geological conditions, most of coal resources are mined underground rather than open-pit². The traditional fully mechanized caving mining method leads to a series of problems such as surface subsidence, destruction of ground buildings, destruction of aquifers, and pollution of the environment by gangue hills³. Academician Qian put forward the concept of “green mining” in 2003, and filling mining has become an effective way to realize the green mining of coal mine disaster reduction and reduction⁴. In addition,

¹College of Mining Engineering, North China University of Science and Technology, Tangshan 063210, Hebei, China.

²College of Emergency Management and Safety Engineering, North China University of Science and Technology, Tangshan 063210, Hebei, China. ³Key Laboratory of Mining Development and Safety Technology in Hebei Province, Tangshan 063210, China. ⁴College of Safety Science and Engineering, Xi'an University of Science and Technology, Xi'an 710054, Shanxi, China. ⁵College of Safety Engineering, China University of Mining and Technology, Xuzhou 221116, Jiangsu, China. ✉email: guoliwen64@163.com; zjy815@163.com

a series of laws, regulations and policy documents such as the reduction of mineral resource tax, the replacement of production capacity and the new solid waste law provide opportunities and guarantees for the development of filling mining. It is imperative to carry out research on backfill mining technology.

Cement paste backfill (CPB) is widely used in underground mines around the world. Traditional paste backfill usually contains ordinary Portland cement (OPC) as a cementing agent, and its cost accounts for 60%~80% of the cost of backfill materials⁵. According to the data of the National Bureau of Statistics, the cement production of China has long ranked first in the world. The national output of cement above scale is 2.02 billion tons, and the corresponding carbon emission is about 1.1 billion tons, accounting for about 12% of the total national carbon emission. In addition, the coal-based solid waste (mainly including coal gangue, furnace bottom slag, fly ash, desulfurization gypsum, etc.) of China has accumulated a stock of tens of billions of tons, with a rapid growth of 1.5 billion tons one year, accounting for more than half of industrial solid waste. The low comprehensive utilization rate and large storage capacity of solid waste lead to the increase of environmental pollution risks such as water, soil and gas, which threatens the safety and health of the public. Therefore, efficiently utilizing solid waste to produce solid waste-based cementitious materials (SWBCM) is one of the most effective ways to achieve the reduction, resource recovery, and harmless disposal of solid waste, which can also lower the filling costs and carbon emissions associated with cement production⁶.

As a new type of low-carbon cementitious material, SWBCM is mainly composed of industrial solid waste such as fly ash (FA), granulated blast furnace slag (GS), steel slag (SS)⁷. However, the low alkalinity environment affects hydration reaction, resulting in a low early strength of SWBCM, which limits its promotion and application⁸. Zhou et al. studied the hydration properties of steel slag-red mud-cement-based composite mortar, and found that a single doped steel slag hindered the hydration process of the composite material, and the early strength of the composite material decreased⁹. At present, chemical alkali activators are often added to improve the strength of SWBCM. However, the traditional alkaline activator solution is mainly composed of sodium silicate (SS) and sodium hydroxide (SH), which is not only expensive but also energy-consuming¹⁰. Compared with the traditional OPC-based concrete mixture, its use will cause environmental problems such as human health risks, freshwater ecotoxicity and a tenfold increase in ozone layer consumption potential¹¹. Based on the high concentration of cemented backfill technology, the effects of several activators on fly ash-based cementitious backfill materials were studied by Yu. The results show that Na_2SiO_3 provides the most effective activation, leading to an increase in strength, while the backfill cost also rises¹². On one hand, using low-modulus water glass can enhance mechanical performance, while it complicates the process, generates significant heat during use, and may lead to issues such as excessively rapid setting times. On the other hand, low-modulus water glass is not easily stored at room temperature and requires on-site preparation. Hence, it is particularly necessary to explore low-cost alkaline substances that can replace traditional alkali activators.

Carbide slag (CS) is an industrial alkaline solid waste produced by the hydrolysis of calcium carbide during the production of polyvinyl chloride. The main component is $\text{Ca}(\text{OH})_2$ (CH), and 1.5~1.9 tons of CS can be produced for each ton of PVC¹³. Due to the lack of effective methods for large-scale waste utilization, CS is mainly stored in open space and reprocessed after long-term drying, resulting in land occupation, waste of calcium resources, soil, groundwater and environmental pollution¹⁴. In fact, CS has small particle size and low pretreatment cost. In recent years, researchers have begun replacing strong alkaline activators with alkaline solid waste to activate potentially reactive aluminosilicate materials for the production of new binders, aiming to reduce costs and address the issue of short curing times caused by strong alkaline activation. Guo used soda residue, CS and ground granulated blast furnace slag to prepare a binder, which can obtain better mechanical properties¹⁵. A new type of low carbon cementitious material was synthesized by Bai et al. using CS, soda residue, red mud and FA as raw materials, the compressive strength has reached 10.7 and 22.1 MPa after sealed curing at room temperature for 3 and 28 days¹⁶. Furthermore, the amount of coal gangue (CG) generated from coal mining and furnace bottom slag (FBS) produced by coal-fired power plants is steadily increasing. The primary disposal methods of CG and FBS are stockpiling and landfilling, which not only occupy land resources but also lead to various environmental pollutants. Chen et al. have shown that fine particles less than 1.25 mm in FBS account for more than 50%, which was beneficial to improve the strength of the filling body and form a dense skeleton structure. Adding an appropriate amount of FBS as fine aggregate in coarse aggregate CG can slow down the crack propagation speed of the filling body under stress¹⁷. The above research provides a certain feasibility theory for reducing the pollution of solid waste to the environment and developing new means of resource utilization.

In summary, while many studies have focused on the preparation of SWBCM from solid waste, information on the use of CS as a solid alkaline activator to replace traditional cement binders is still limited. Furthermore, there is less research on the preparation of GBC for mine backfill using coal-based solid waste, such as CG and FBS, as aggregates, in conjunction with GS and CS as cementitious materials, especially in a full-solid waste system. The synergistic effects between GS and CS, the mechanical properties and failure mechanisms of mine backfill materials, the solidification ability of heavy metal ions, and cost-effectiveness have been less explored. Therefore, GS was used as an aluminosilicate raw material, CS as an alkaline activator, and CG and FBS as aggregates to prepare full-solid waste backfill materials GBC by leveraging the complementary advantages of these solid wastes. The hydration products of GCCM were characterized using X-ray diffraction (XRD), in-situ Fourier-transform infrared spectroscopy (in-situ FTIR), scanning electron microscopy with energy dispersive spectroscopy (SEM-EDS), thermogravimetric analysis (TG-DTG) and Brunauer–Emmett–Teller (BET) methods, and the synergistic hydration mechanism of GCCM was revealed. The mechanical properties of the GCCM and GBC were tested through unconfined compressive strength (UCS) tests. Additionally, the working characteristics, environmental impact and cost-effectiveness of GBC were studied by varying the content of GCCM. This research aligns with the concepts of “treating waste with waste” and “treating disaster with waste”, and promotes the use of multi-source solid waste for preparing mine backfill materials, which significantly

Type	Mad/%	Vad/%	FCad/%	Aad/%
FBS	0.58	1.72	1.63	96.07
CG	1.49	11.46	8.80	78.25

Table 1. Industrial analysis results of aggregates.

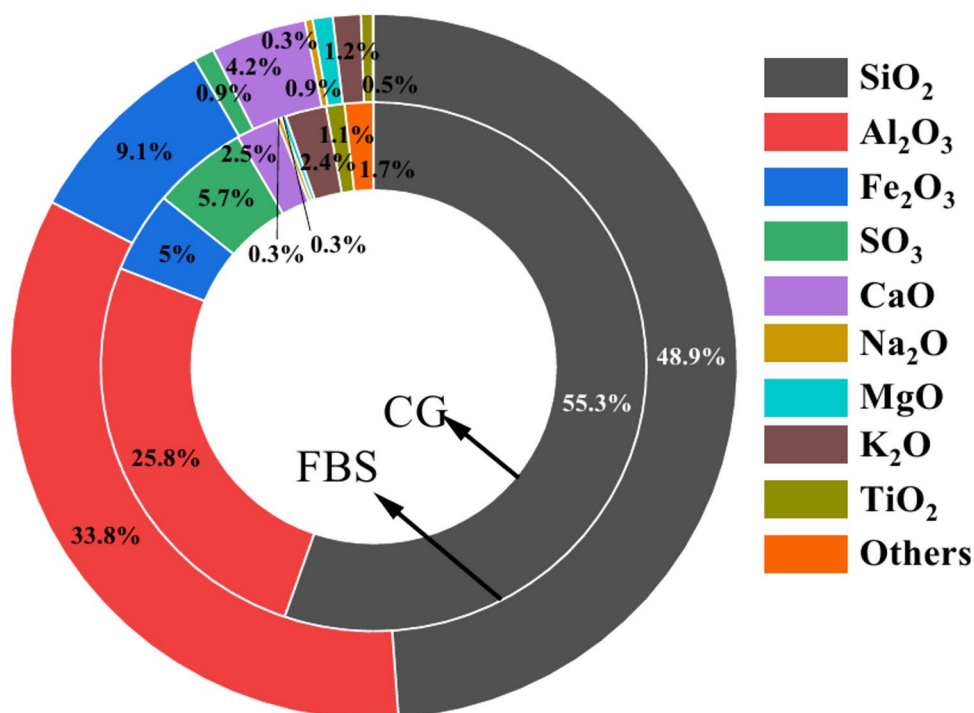


Fig. 1. The proportion diagram of chemical composition of aggregate.

reduces the carbon emissions associated with Portland cement production. The approach also offers advantages such as the use of local materials, cost-effectiveness and environmental sustainability.

Experimental materials and properties

Solid waste and mixing water were used as the main experimental raw materials, including CG, FBS, GS and CS, and the mixing water was laboratory tap water.

Aggregate

CG is taken from a coal mine in Tangshan, and FBS is provided by a coal-burning power plant. The industrial analysis data of CG and FBS are shown in Table 1. The results indicate that the moisture, volatile matter, and fixed carbon content of CG are higher, while the ash content is lower. In contrast, the composition of FBS shows the opposite trend. This can be attributed to the fact that FBS primarily consists of residues remaining after combustion, with most of the volatile components having been eliminated during the process.

The XRD test results of the aggregate are shown in Fig. 1. The main components of FBS and CG are SiO_2 , Al_2O_3 , CaO , Fe_2O_3 , K_2O and TiO_2 , accounting for 92.0 and 97.8% of the total components in FBS and CG, respectively. The FBS used in the experiment is mainly composed of quartz and mullite¹⁸. The main component of CG is quartz, which belongs to clay coal gangue. A large amount of SiO_2 ensures the high hardness and deformation resistance of CG.

Cementitious materials

GS was purchased from Henan Wuhu Environmental Protection Technology Co., Ltd., which is a by-product of blast furnace ironmaking and serves as the main silicon-rich aluminate precursor. The appearance of GS is grayish white solid powder, the flow ratio is 97%, and the activity indexes of 7d and 28d are 84.1 and 98.3%, separately. The density is 3.10 g/cm^3 , the loss on ignition is 0.87%, and the water content is 0.43%. After drying (105°C drying to constant weight) and sieving (200 mesh standard sieve), XRF, XRD and SEM tests were carried out to determine the chemical composition, mineral composition and microstructure of the raw materials. As shown in Fig. 2, the main chemical components of GS are SiO_2 , Al_2O_3 and CaO , and the calculated alkaline coefficient M_0 is 0.77, which belongs to acidic slag; the mass coefficient K is 1.62, which belongs to high active slag. The XRD pattern in Fig. 3 of GS has a “steamed bread peak” at $20^\circ \sim 40^\circ$, showing a typical diffuse diffraction

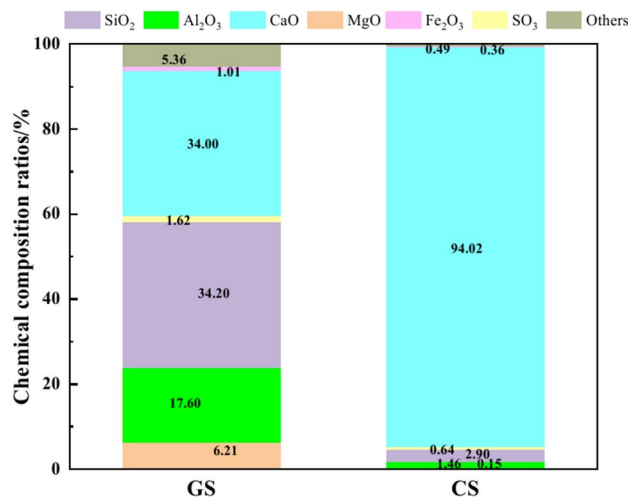


Fig. 2. The chemical composition ratios of GS and CS.

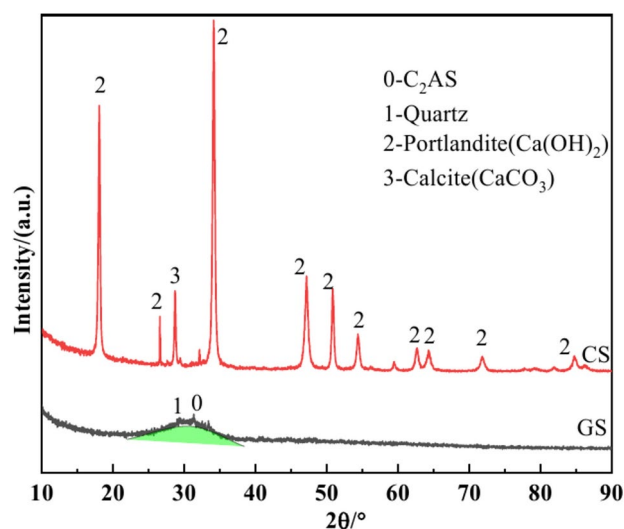


Fig. 3. XRD spectrum of GS and CS.

pattern of amorphous glassy materials, with a small amount of crystalline compounds SiO₂, calcite (CaCO₃) and gehlenite(C₂AS). The GS structure in Fig. 4A is mainly cryptocrystalline, showing irregular prismatic and flaky.

CS was provided by a chlor-alkali company in Tangshan province. After standing for 7 days, the CS slurry exhibited a layered structure, with a colorless, clear alkaline solution on top, primarily composed of CH, and a lower layer of CS slurry, which had a wet basis moisture content of 89.58%. The main chemical components of CS are CaO, along with small amounts of SiO₂ and Al₂O₃. The M_0 of CS is 21.63, categorizing it as an alkaline waste residue. The K of CS is 31.75, significantly higher than that of GS. This indicates that, under a specific blend of cementitious materials, CS can provide suitable hydration activity and strength development effects for GS. XRD analysis shows that the primary crystalline compounds are CH and minor amounts of calcium carbonate (CaCO₃). SEM images in Fig. 4B reveal that CS mainly consists of a loose block structure with numerous platy crystal forms of CH, while CaCO₃ crystals are present in granular or microcrystalline forms within the CS.

Figure 5 shows the infrared spectra of GS and CS. The broad absorption peak at 3423 cm⁻¹ corresponds to the stretching vibration of the -OH bond in H₂O, while the weak absorption peak at 1639 cm⁻¹ is caused by the bending vibration of -OH, reflecting the internal vibrational absorption characteristics of the water within the crystals. The absorption peak near 1430 cm⁻¹ is attributed to the asymmetric stretching vibration of the C-O bond¹⁴. In the low-frequency region of the GS spectrum, the absorption peaks at 450~700 and 956 cm⁻¹ correspond to the silicoaluminate groups in GS, representing the presence of Al-O and Si-O bonds, respectively¹⁶. In the CS spectrum, the absorption peaks of CH appear at 3639 cm⁻¹ (stretching vibration of the -OH group) and 1624 cm⁻¹ (bending vibration of H-O-H), while the absorption peak at 869 cm⁻¹ for carbonate is generated by the symmetric stretching vibration of CO₃²⁻⁶.

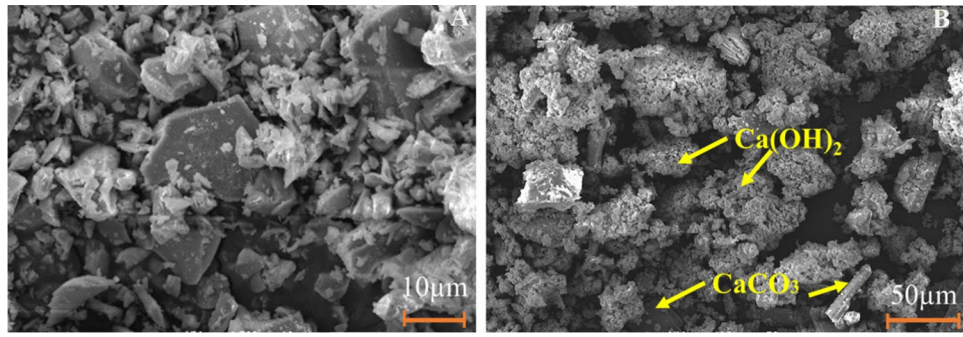


Fig. 4. SEM images of GS and CS (A: GS; B: CS).

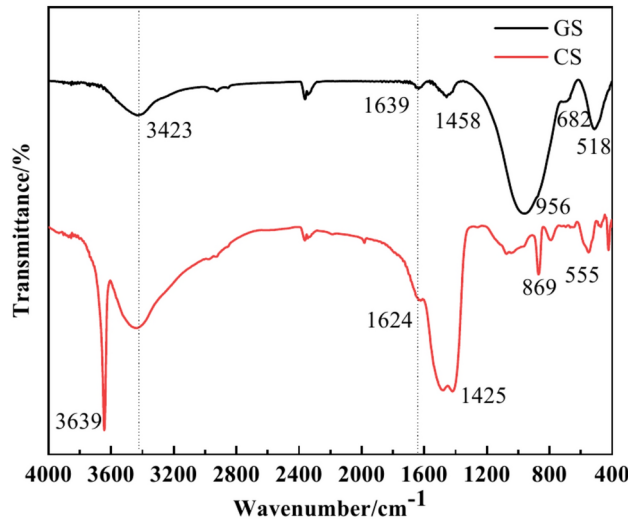


Fig. 5. FTIR spectra of GS and CS.

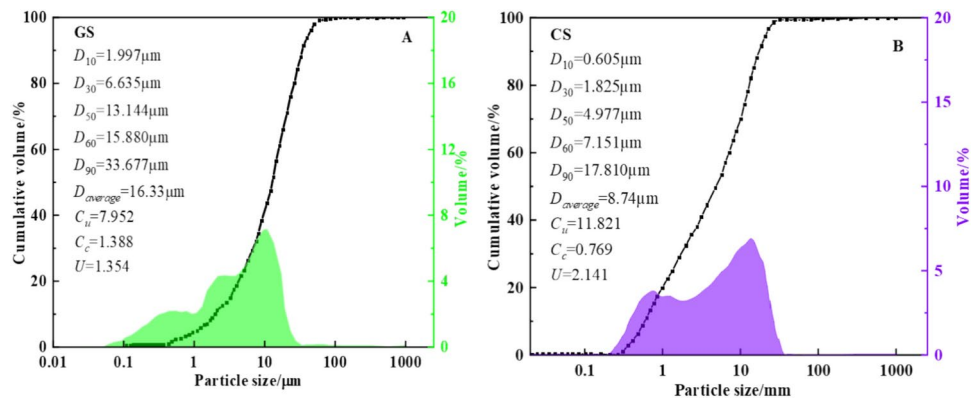


Fig. 6. The particle size distribution of GS and CS.

The particle size distribution of GS and CS are shown in Fig. 6. The median particle sizes of GS and CS are 13.144 and 4.977 µm, respectively. The smaller particle size of CS allows it to effectively fill the voids in GS, facilitating the activation of alkali reactions. Based on formulas $C_u = \frac{D_{60}}{D_{10}}$ and $U = \frac{D_{90}-D_{60}}{D_{50}}$, the uniformity coefficients of GS and CS are 7.952 and 11.821, respectively, with curvature coefficients C_c of 1.388 and 0.769. These values indicate that GS exhibits good particle size distribution, while CS demonstrates poor grading. The grading uniformities (U) are 1.354 and 2.141, separately. Since the multimolecular layer adsorption theory (BET theory) method does not require assumptions about particle shape or semi-empirical formulas¹⁹, the specific

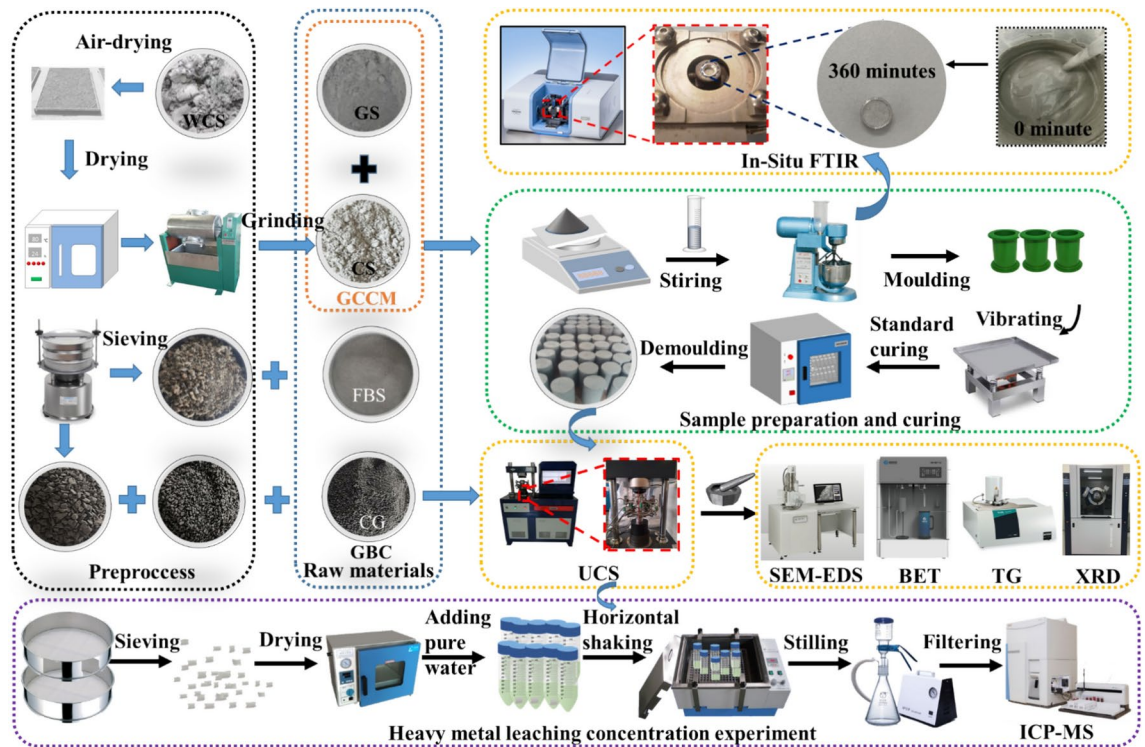


Fig. 7. Schematic diagram of experimental process.

Samples ID	Raw materials/ wt. %		Element molar ratio of mixture slurry		Water-cement ratios (mL/g)	Curing condition
	GS	CS	$n(\text{CaO})/n(\text{SiO}_2)$	$n(\text{CaO})/n(\text{SiO}_2 + \text{Al}_2\text{O}_3)$		
G9C0	93	7	1.279	0.388	0.5	$20 \pm 1^\circ\text{C}$, $90 \pm 5\% \text{R.H}$
G8C1	83	17	1.640	0.499		
G7C2	73	27	2.089	0.635		
G6C3	63	37	2.663	0.808		
G5C4	53	47	3.421	1.042		

Table 2. GCCM experimental mixing ratio. # G*C*: G in G* is GS, * is the percentage of GS content in GCCM, C in C* is CS, * is the percentage of CS content in GCCM.

surface areas were measured using nitrogen adsorption. The specific surface area of GS is $1.585\text{m}^2/\text{g}$, while that of CS is significantly higher at $23.371\text{m}^2/\text{g}$, indicating a much greater surface area for CS.

Experimental scheme and method

Experimental scheme

The strength development of GCCM primarily relies on the hydration reactions of GS and CS. To investigate the hydration reactions of GCCM cementing system and the synergistic reaction mechanism between the GS and CS, GCCM was prepared using GS and CS as raw materials without interference from filler aggregates. Referring to the previous studies and a large number of experimental studies^{6,20,21}, the mass ratios of GS to CS were set at 93:7, 83:17, 73:27, 63:37, and 53:47, and the solid concentration was 66.6% (water-to-solid ratio of 0.5). The schematic diagram of test process was shown in Fig. 7. CS in wet slurry state (WCS) was subjected to air-drying, oven-drying, and grinding for pretreatment. Then, dried GS, CS, and tap water were weighed according to the proportions listed in Table 2 and mixed by mechanical stirring for 3 min until a homogeneous slurry was obtained. The fresh slurry was poured into cylindrical molds with dimensions of $\Phi 50\text{mm} \times 100\text{mm}$ (D×H), and vibration was applied on a vibrating table for 60 s to eliminate air bubbles. The molds were covered with cling film and placed in a constant-temperature and constant-humidity curing chamber ($95 \pm 1\% \text{RH}$, $20 \pm 1^\circ\text{C}$). After 24 h, the specimens were demolded and cured to the required age. The in-situ infrared conversion of GCCM fresh grout with optimal strength at 28 days was monitored during the early hydration stages. UCS tests were conducted on the GCCM samples at 3, 7, 14 and 28 days of curing. The microstructural properties of the hydration products of GCCM were characterized using XRD, SEM-EDS, BET and TG analyses.

Based on the optimal 28d UCS mix ratio of GCCM, and drawing on previous studies and preliminary experiments²¹, GBC series samples with a mass concentration of 77% (water-to-solid ratio of 0.3) were prepared, with mixing and curing conditions identical to those of GCCM. CG and FBS aggregates were sieved and weighed according to the proportions shown in Table 3. Specifically speaking, FBS was passed through a 0.8 mm standard square-hole sieve as a fine aggregate. GS was sieved to obtain GS with particle size range of 0~2, 2~5 and 5~10 mm as coarse aggregate. The principle of 1/5 of the minimum diameter is introduced, assuming that the total mass of aggregate required for the preparation of a standard sample is M_t , the aggregate mass required for the particle size range between d_1 and d_2 satisfies the following formula²²:

$$M_{d_1}^{d_2} = \left[\left(\frac{d_2}{d_{\max}} \right)^n - \left(\frac{d_1}{d_{\max}} \right)^n \right] M_t \quad (1)$$

where: d_{\max} represents the maximum particle size, which takes 10 mm, n represents the Talbot gradation index, which takes 0.4.

GBC was prepared with FBS:CG = 1:1, and the proportion of CG aggregates in different particle size ranges was 52.5, 23.3 and 24.2%, respectively. The slump and extensibility of the fresh GBC slurry were measured using the mini slump test. After 28 days of curing, the leaching characteristics of heavy metal ions from GBC specimen were studied to preliminarily assess the filling properties and feasibility of producing GBC from full-solid waste.

Experimental method

Industrial analysis: The industrial components such as moisture, volatile matter, ash, and fixed carbon in CG and FBS were determined using a fully automatic industrial analyzer (5E-MAG6700, Changsha Kaiyuan Instruments Co., Ltd., China). Each sample was tested three times, and the average values were recorded.

Particle size distribution: Using anhydrous ethanol as a dispersing medium, the particle size distribution of GS and CS was analyzed with a laser particle size analyzer (NRTG100-D, Shandong Niket Analytical Instrument Co., Ltd., China).

XRD: Mineral composition analysis of GCCM was performed using an X-ray diffractometer (D8 Advance, Bruker, Germany) with a Cu target, operating at 40 kV and 20 mA. The 2θ scanning range was from 10° to 90° , with a scanning speed of $5^\circ/\text{min}$ and a step size of 0.01° .

FTIR: The molecular structure and functional group changes of GS and CS were analyzed using a Fourier-transform infrared spectrometer (VERTEX70, Bruker, Germany) via KBr pellet method in the transmission mode within the range of 4000 to 400 cm^{-1} .

SEM-EDS: A scanning electron microscope (JEOL JSM-IT100A, Japan) coupled with Energy Dispersive Spectroscopy (EDS) was used for observing the microstructure and surface elemental composition of GS, CS, GCCM and GBC 30. After compressive strength testing, small blocks from the axial positions of GCCM and GBC samples at different ages and ratios were crushed and immersed in anhydrous ethanol to terminate hydration for 7 days. The samples were then placed in a vacuum drying oven for 12 h. Representative specimens, with a flat upper and lower surface and a height not exceeding 2 mm, were gold-sputtered for morphological and energy spectrum analysis.

Flowability: According to GB/T 8077-2012, freshly mixed solid waste slurry of GCCM was placed into a frustum-shaped mold, and the upper surface was leveled with a spatula. The timing started when the mold was vertically lifted, lasting for 30 s. The average sum of the maximum horizontal and vertical diameters of the flattened slurry was taken as the result for one flowability test, with three tests conducted for each ratio to obtain the average value.

Bleeding rate: The bleeding rate was determined by the ratio of the volume of water that separated from the slurry of GCCM after standing for 1 h to the original water content of the slurry.

Compressive strength and elastic modulus: The uniaxial compressive strength and elastic modulus of GCCM and GBC at the specified curing age were tested using an elastic modulus device (HTB-2, Jinan Mineral Rock Testing Instrument Co., LTD, China). The sample dimensions were $\Phi 50 \text{ mm} \times 100 \text{ mm}$, with a loading speed of 0.05 kN/s . The average values of three samples' test results were recorded as the strength value²³.

In-situ Infrared: An in-situ diffuse reflectance Fourier-transform infrared spectrometer (INVENIO S, Bruker, Germany) was employed to measure the in-situ transformation of the fresh slurry of GCCM ($n(\text{CaO})/n(\text{SiO}_2 + \text{Al}_2\text{O}_3) = 0.635$) during curing in the range of 600 to 4000 cm^{-1} . This involved using a Harrick diffuse reflectance accessory and a low-temperature nitrogen-cooled MCT/B optical detector. The temperature was maintained at 25°C , with a monitoring duration of 360 min. The thoroughly mixed GS-CS slurry was immediately placed into a small crucible positioned centrally on the sample stage, with the optical path adjusted to achieve a reflection intensity between 2 and 9.8.

Samples ID	GBC25	GBC30	GBC35	GBC40
GCCM	25	30	35	40
FBS+CG	75	70	65	60

Table 3. Experimental mixing ratio of GBC (wt.%). # GBC* indicates that the GCCM content accounts for *% of the total solid mass.

Thermogravimetric Analysis: A synchronous thermal analyzer (PerkinElmer STA 6000, USA) was used to assess the thermogravimetric (TG) curve of the hydration products of GCCM in a nitrogen atmosphere, heating from room temperature (30 °C) to 1000 °C at a rate of 20 °C/min.

BET: The specific surface area of the hydration products of GCCM was calculated using a BET surface area analyzer (BK112T, Beijing Jingwei Gaobo Technology Co., Ltd., China) based on the adsorption/desorption curves, and the pore sizes of the materials were calculated using the BJH model based on the nitrogen desorption data.

Slump: A mini slump cone ($\Phi 5\text{cm} \times \Phi 10\text{cm} \times 15\text{cm}$) was utilized to evaluate the flow performance of GBC. The slump cone was pre-wetted, and the freshly mixed slurry was placed inside the cone and compacted in three stages with a tamper. Excess slurry on the surface was scraped off with a spatula. The height of the slurry vertical drop was measured as the “slump” with results averaged over three tests. The horizontal spread distance was measured as the “expansion”, following the same calculations as the flowability testing.

Heavy metal leachate concentration: In accordance with GB 18,599-2020, leachate was prepared from GBC samples that had been solidified for 28 days (crushed and screened through a 3 mm sieve) and their raw materials according to national standard HJ 557-2010. The concentrations of heavy metal ions in the leachate were detected using an Inductively Coupled Plasma Mass Spectrometer (ICP-MS, Agilent 7700, Shanghai Xiyan company, limited, China) and compared to the GB 8978 comprehensive discharge standard for wastewater²⁴.

Results and analysis

Analysis of synergistic reaction mechanism of GCCM

Analysis of mineral composition of hydration products

The XRD patterns of G7C2 at different ages are shown in Fig. 8. Compared with the XRD patterns of GS and CS (Fig. 3), new hydration products, such as AFm, amorphous C-(A)-S-H, and hydrotalcite (HT), were observed in GCCM. This suggests that CS promotes the hydration of GS, which is consistent with the findings of Zhang et al.²⁵. Specifically, CS provides a highly alkaline environment for the hydration of GS²⁶. Under the alkaline activation of CS, Ca^{2+} , Mg^{2+} , SiO_4^{4-} and Al^{3+} ions are released from GS. These ions combine with SO_4^{2-} and CO_3^{2-} in the alkaline and high calcium environment to form hydration products such as AFm, C-(A)-S-H and HT²⁷. As shown in Fig. 8A, with the extension of curing time (from 3 to 14 days), the intensity of the CaCO_3 diffraction peaks gradually decreases, the intensity of the CH diffraction peaks slightly decreases. While the diffraction peaks of AFm crystals and HT gradually increase, and the area of the prominent “hump” between 20° and 40° increases. This indicates that the partial dissolution of CaCO_3 and CH promotes the formation of hydration products such as AFm, hydrotalcite and C-(A)-S-H gel. Additionally, the higher calcium content in CS promotes the crystallization of CH in the alkaline environment, CH undergoes carbonation, leading to the formation of CaCO_3 ²⁸, while CH and CaCO_3 primarily derived from the raw material CS.

As the curing time reaches 28 days, the intensity of the CaCO_3 diffraction peaks increases, primarily due to the carbonation of CH, which leads to an increase in the amount of CaCO_3 . As shown in Fig. 8B, with the increase in the molar ratio of $n(\text{CaO})/n(\text{SiO}_2 + \text{Al}_2\text{O}_3)$, the area of the prominent “hump” initially increases and then decreases. This suggests that the amount of C-(A)-S-H gel increases at first and then decreases. The increase in CS content raises the alkalinity of the system, promoting the hydration reaction of GS and favoring the formation of more hydration products. However, when the ratio of $n(\text{CaO})/n(\text{SiO}_2 + \text{Al}_2\text{O}_3)$ exceeds 0.635, the high alkalinity environment induced by CS causes an excess of OH^- ions, which preferentially react with Ca^{2+} to form CH, leading to its crystallization on the GS surface. This inhibits the hydration reaction to some extent, resulting in a decrease in gel content⁶.

Analysis of in-situ structural transformation of hydration products

Figure 9 shows the in-situ infrared spectra changes of GCCM with a $n(\text{CaO})/n(\text{SiO}_2 + \text{Al}_2\text{O}_3)$ ratio of 0.635 over reaction times within 360 min. The analysis reveals that, as shown in Fig. 9A, the absorption peak at 1141 cm^{-1}

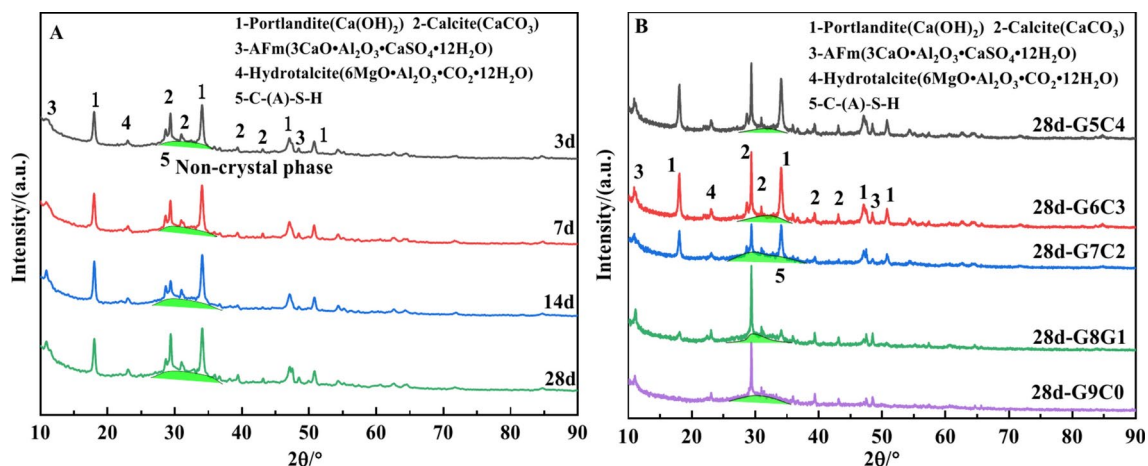


Fig. 8. XRD patterns of GCCM samples. (A) Different ages of G7C2; (B) Different $n(\text{CaO})/n(\text{SiO}_2 + \text{Al}_2\text{O}_3)$.

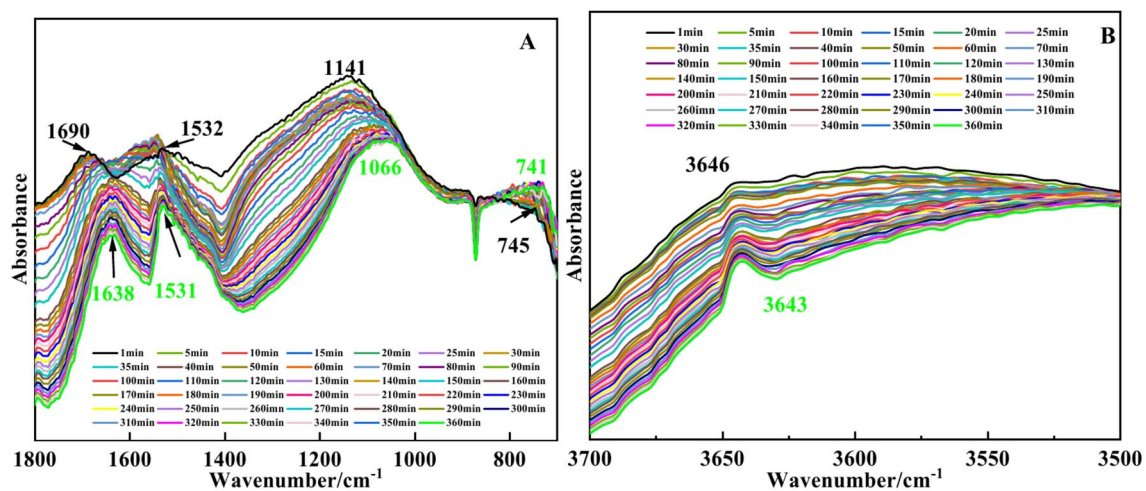


Fig. 9. In-situ infrared spectra of GCCM. (A) 700 ~ 1800 cm^{-1} ; (B) 3500 ~ 3700 cm^{-1} .

shifts to 1066 cm^{-1} after 360 min. On one hand, under the alkaline activation of CS, the amorphous phase of the silicates in GS dissolves, causing the Si-O-Si(Al) bonds at 1141 cm^{-1} to break. As the hydration time increases, the number of chemical bonds contributing to the absorption peak gradually decreases, resulting in a continuous decrease in the peak intensity²⁹. On the other hand, after the Si-O-Si(Al) bonds are broken, the electron cloud distribution around the oxygen atoms in the $[\text{SiO}_4]$ and $[\text{AlO}_4]$ tetrahedra undergoes significant changes. This alteration in the electron cloud distribution affects the vibrational characteristics of the chemical bonds, causing the absorption peak to shift to 1066 cm^{-1} , where it exhibits Si(Al)-O stretching vibrations. This change indicates a reduction in the polymerization degree of the $[\text{SiO}_4]$ and $[\text{AlO}_4]$ tetrahedra, which is inferred to result from the incorporation of CS, promoting the formation of a large amount of low-polymer gel structures containing more C-(A)-S-H gel³⁰. In addition, the absorption peak of the CO_3^{2-} group at 745 cm^{-1} exhibits a shift to lower wavenumbers and a gradual increase in intensity, which is related to the carbonation reaction of CH²⁶. The absorption peak at 1532 cm^{-1} becomes progressively sharper and more pronounced with the prolongation of the hydration time, which may be attributed to the increasing densification of the hydrogen bonding network in the hydration products as the hydration reaction proceeds³¹. Furthermore, the band at 1690 cm^{-1} is attributed to the asymmetric stretching vibration of H-O-H in free water, typically present in the form of liquid water or adsorbed water³². However, after 360 min, this band shifts to 1638 cm^{-1} , which is assigned to the bending vibration of H-O-H, reflecting the presence of hydroxyl structures in the C-(A)-S-H gel^{33,34}. In Fig. 9B, the absorption peak at 3643 cm^{-1} corresponds to the O-H bond vibration in CH³⁵. It is observed that the intensity of this absorption peak increases with the extension of the hydration reaction time, which may be related to the transformation of CH from an amorphous to a crystalline state. These findings also support the progression of the hydration reaction and corroborate the XRD results.

Microscopic morphology analysis of hydration products

When the ratio of $n(\text{CaO})/n(\text{SiO}_2 + \text{Al}_2\text{O}_3)$ is 0.635, the microstructural morphology of GCCM at different curing ages is illustrated in Fig. 10. It can be observed that the microstructure of GCCM is characterized by complex arrangements of flaky, layered, and network-like amorphous structures. In Fig. 10A, influenced by the early curing age and incomplete hydration reactions, the structure appears relatively loose with numerous irregular voids. The surface displays layered structures, hexagonal plate-like CH crystals approximately a few micrometers wide, as well as some GS particles that have been partially corroded by alkalis. Additionally, the presence of cross-linked, honeycomb-like, and fibrous C-(A)-S-H gel is a primary contributor to the formation of the three-dimensional network structure and overall strength. In Fig. 10B–F, as the curing age increases, the quantity of C-S-H gel and C-A-S-H gel (as confirmed by EDS analysis) increases, leading to the formation of gel particles with irregular shapes and similar sizes. These particles further accumulate and interconnect, resulting in a denser microstructure. Concurrently, the amount of CH decreases, and the surface of the samples shows a significant presence of petal-like AFm crystals (Fig. 16F) along with a small quantity of cubic CaCO_3 . The interlocking of hydration products serves as a filler and reduces voids, contributing to a more compact microstructure that favors the strength development of GCCM³⁶. Furthermore, as the ratio of $n(\text{CaO})/n(\text{SiO}_2 + \text{Al}_2\text{O}_3)$ increases, the number of pores in GCCM initially decrease and then increase. The samples in Fig. 10a,c exhibit a loose internal structure compared to Fig. 10b. This is because when the $n(\text{CaO})/n(\text{SiO}_2 + \text{Al}_2\text{O}_3)$ ratio is low, the CS content is limited, and the lower alkalinity environment results in fewer GS hydration products, which affects the structural densification of GCCM. Conversely, when the ratio of $n(\text{CaO})/n(\text{SiO}_2 + \text{Al}_2\text{O}_3)$ is 1.042, the high alkalinity environment promotes the preferential precipitation of CH crystals, leading to a relative reduction in the hydration products, which is consistent with the XRD results.

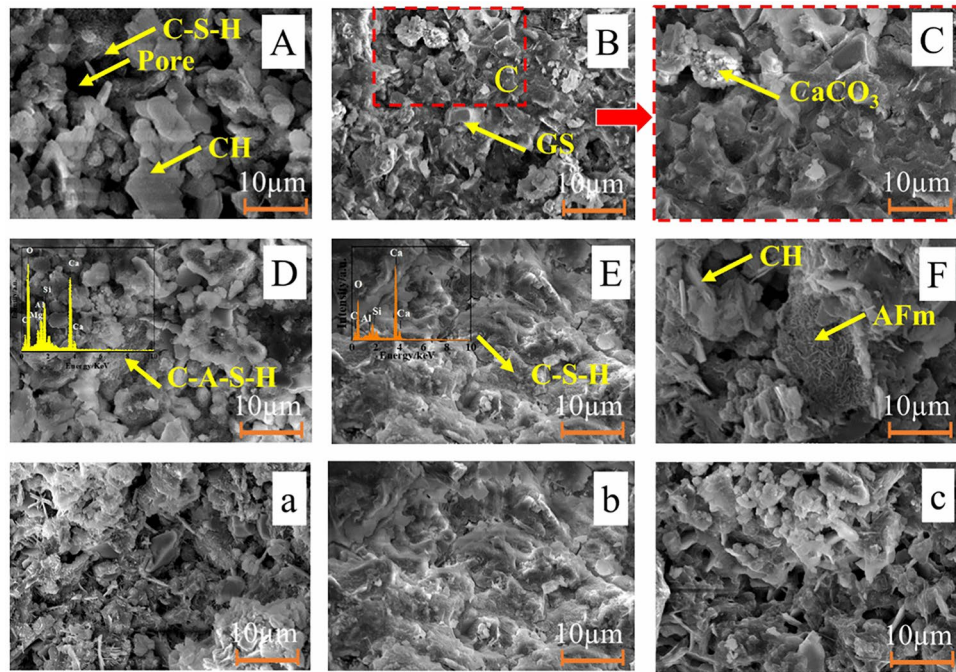


Fig. 10. SEM image of GCCM. (A) G7C2 of 3d age; (B,C) G7C2 of 7d age; (D) G7C2 of 14d age; (E,F) G7C2 of 28d age; (a) $n(\text{CaO})/n(\text{SiO}_2 + \text{Al}_2\text{O}_3) = 0.388$; (b) $n(\text{CaO})/n(\text{SiO}_2 + \text{Al}_2\text{O}_3) = 0.635$; (c) $n(\text{CaO})/n(\text{SiO}_2 + \text{Al}_2\text{O}_3) = 1.042$.

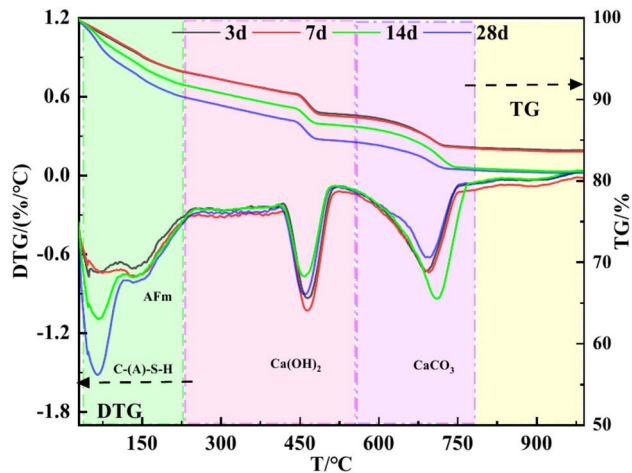


Fig. 11. TG-DTG curves of G7C2 at different ages.

Thermogravimetric analysis of hydration products

Figure 11 presents the TG and DTG curves of GCCM ($n(\text{CaO})/n(\text{SiO}_2 + \text{Al}_2\text{O}_3) = 0.635$) at different curing ages. The TG curve exhibits a continuous decline, while the DTG curve reveals four distinct weight loss peaks. Notably, the weight loss peaks in the temperature ranges of 30–130 °C and 130–200 °C are significantly different. These ranges are attributed to the decomposition of hydration products C-(A)-S-H and AFm, as well as the evaporation of physically bound water, which are closely related to the sample composition³⁷. The weight loss occurring between 200 and 550 °C is associated with the dehydroxylation of CH. Meanwhile, the weight loss peak in the 550–750 °C range corresponds to the thermal decomposition of CaCO_3 , arising either from CS or from carbonation during the solidification of GCCM and CH³⁸. As shown in Table 4, with the increase in curing age, the mass loss rate of hydration products and CaCO_3 significantly increases, which is related to the increased formation of C-(A)-S-H gel, AFm, and the carbonation of CH into CaCO_3 . The presence of the weight loss peak again confirmed the formation of hydration products, which was consistent with XRD and in-situ FTIR results.

Figure 12 illustrates the TG-DTG curves for GCCM samples cured for 28 days at varying $n(\text{CaO})/n(\text{SiO}_2 + \text{Al}_2\text{O}_3)$ ratios. The characteristic absorption peaks are consistent with those in Fig. 11. To quantitatively analyze the

Ages	$M_{C-(A)-S-H\&AFm}$	M_{CH}	M_{CaCO_3}
3d	5.608	5.878	3.653
7d	5.644	5.864	3.932
14d	7.237	5.620	4.459
28d	8.928	5.423	4.831

Table 4. Mass loss rate of hydration products in G7C2.

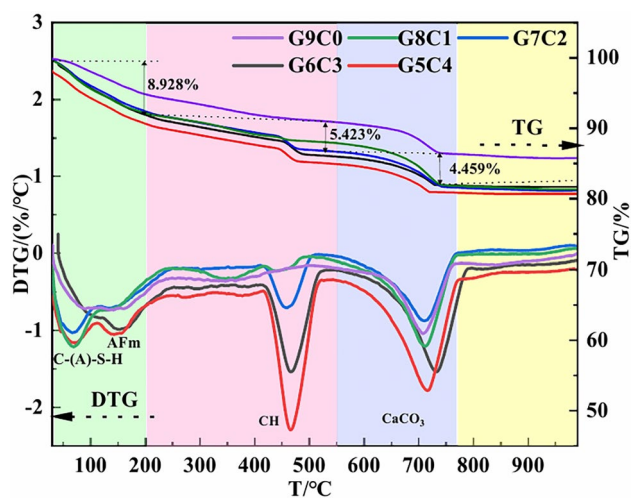


Fig. 12. TG-DTG curve of GCCM.

Samples ID	M_1	M_2	M_3	α
G9C0	4.772	3.221	4.371	40.771
G8C1	6.510	4.064	5.871	54.087
G7C2	8.928	5.423	4.459	67.413
G6C3	6.605	5.643	4.167	58.151
G5C4	6.347	5.745	3.947	57.126

Table 5. Mass loss rate and hydration degree of hydration products.

impact of $n(\text{CaO})/n(\text{SiO}_2 + \text{Al}_2\text{O}_3)$ on the hydration degree of GCCM, the content of hydration products based on the thermal mass loss of C-(A)-S-H, AFm, CH, and CaCO_3 in the 28d hydration system were calculated. The calculation formula are as follows³⁹:

$$M_c = M_1 + M_2 + 0.41M_3 \quad (2)$$

$$\alpha = \frac{M_c}{0.24} \quad (3)$$

$$w(\text{CH}) = M_2 \times \frac{74}{18} \quad (4)$$

$$w(\text{CaCO}_3) = M_3 \times \frac{100}{44} \quad (5)$$

where: M_1 is the mass loss rate due to the decomposition of hydration products C-(A)-S-H and AFm, M_2 is the mass loss rate associated with the thermal decomposition of CH, M_3 is the mass loss rate corresponding to the decomposition of CaCO_3 , M_c represents the mass loss rate of chemically bound water in the cementitious material; $w(\text{CH})$ and $w(\text{CaCO}_3)$ denote the contents of CH and CaCO_3 in the hydration reaction system, respectively, α is the degree of hydration.

The loss rate of weight loss and hydration degree for GCCM is shown in Table 5. As the ratio of $n(\text{CaO})/n(\text{SiO}_2 + \text{Al}_2\text{O}_3)$ increases, the mass loss rate of M_1 and the degree of hydration (α) first increases and

Samples ID	Percentage of pore size/%			BET surface area / (m ² /g)	Pore volume / (cm ³ /g)	Adsorption average pore size / nm
	Micropores / nm 0.50 ~ 2.00	Mesopores / nm 2.00 ~ 50.00	Macropores / nm 50.00 ~ 100.00			
G5C4	1.77	73.69	24.54	30.650	0.094	15.589
G6C3	0.99	71.07	27.95	31.554	0.118	14.930
G7C2	1.07	66.54	32.39	32.839	0.178	12.225
G8C1	0.53	63.20	36.28	28.656	0.174	21.329
G9C0	0.55	61.12	38.33	27.958	0.149	24.286

Table 6. Performance of hydration products of GCCM in BET analysis.

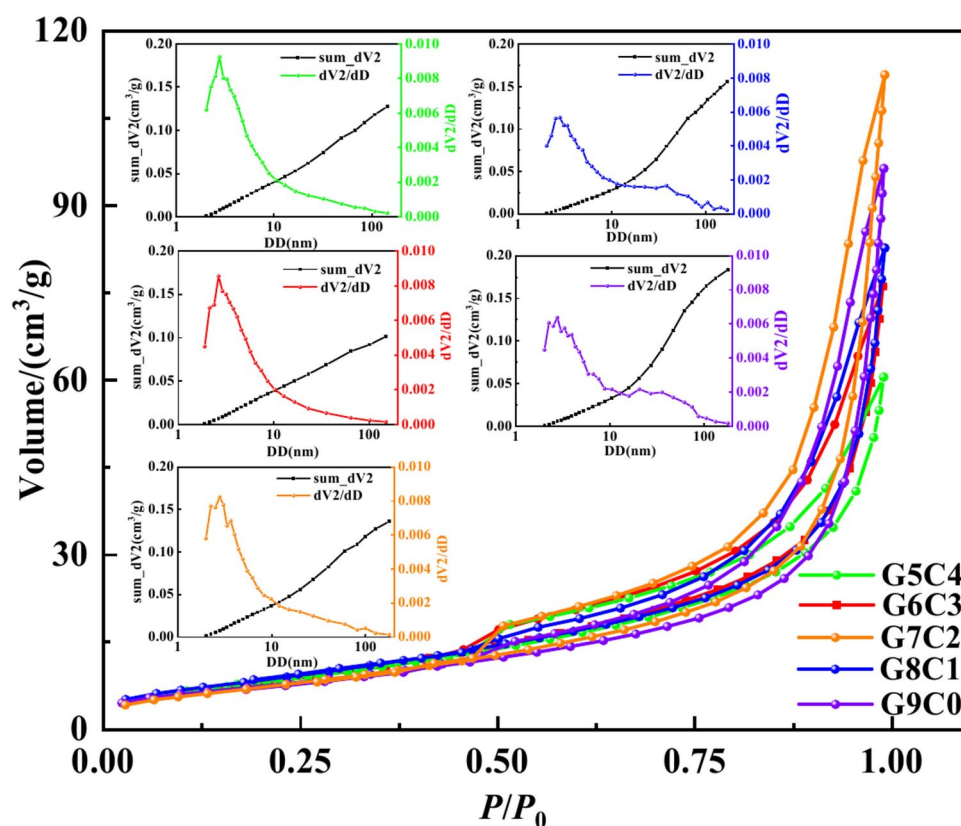


Fig. 13. N₂ adsorption–desorption isotherms and pore size distribution curves of GCCM.

then decreases, the sample with a molar ratio of $n(\text{CaO})/n(\text{SiO}_2 + \text{Al}_2\text{O}_3) = 0.635$ exhibits the highest hydration degree ($\alpha = 67.413$), which is consistent with the XRD and SEM results.

BET analysis of hydration products

After 28 days of hydration, the specific surface area and pore size test results of the GCCM at different $n(\text{CaO})/n(\text{SiO}_2 + \text{Al}_2\text{O}_3)$ ratios are summarized in Table 6. The N₂ adsorption specific surface area ranged from 27.958 to 32.839 m²/g, while the total pore volume varied between 0.094 and 0.174 cm³/g. The average pore size ranged from 12.225 to 24.286 nm. All GCCM samples exhibit abundant mesopores (61.12 to 73.69%), a significant number of macropores (24.54 to 38.33%), and a small amount of micropores (0.53 to 1.77%). A positive correlation was observed between the specific surface area and total pore volume of the samples, while a negative correlation was found with the average pore size. This indicates that the development of the pore structure in GCCM has a direct impact on both the internal specific surface area and pore volume. The GCCM with an $n(\text{CaO})/n(\text{SiO}_2 + \text{Al}_2\text{O}_3)$ ratio of 0.635 exhibited a relatively high specific surface area, total pore volume, and smaller average adsorption pore size, measuring 32.839 m²/g, 0.178 cm³/g, and 12.225 nm, respectively.

The N₂ adsorption–desorption isotherms and pore size distribution for each sample are illustrated in Fig. 13. The results indicate that the hydration products of GCCM display a type IV adsorption isotherm, suggesting the presence of a porous adsorbent exhibiting capillary condensation in a binary composite system. Additionally, the intermediate region contains H₂-type hysteresis loops, primarily caused by the presence of layered particles. This suggests that the pore structure predominantly comprises cylindrical, planar, slit-shaped pores and wedge-

shaped pores, with no distinct saturation adsorption plateau, indicating that the pore structure is irregular¹⁹. This is due to the presence of hydration products in different forms, particularly flocculent, fibrous, honeycomb-like, and gel-like C-(A)-S-H, which have a porous network structure, as well as plate-like CH and petal-like AFm, among others. These findings regarding the pore structure are consistent with the microstructural characteristics observed through SEM.

Synergistic hydration mechanism of GCCM

The microscopic characterization of GCCM hydration products showed that there is a synergistic hydration reaction between GS and CS. In the hydration system, GS serves as a reactive raw material containing silica and alumina, while CS acts as an alkaline activator, providing a conducive alkaline environment and a calcium source that favors the hydration process. The activation effect of CS on GS is noteworthy, with the GCCM slurry primarily engaging in chemical reactions among the amorphous glass phase, C₂AS and portlandite.

The reaction mechanism diagram of the GCCM is illustrated in Fig. 14. When CS dissolves in water, it generates a high pH environment by releasing OH⁻ and Ca²⁺ ions (as shown in Reaction (1)). CS continuously provides GS with a rich alkaline environment, the silica-oxygen protective layer on the surface of GS is damaged, causing the release of Ca²⁺ and Mg²⁺ ions from GS. Under long-term exposure to a strongly alkaline environment, the glassy network structure of the silica-alumina phase in GS gradually depolymerizes, which facilitates the cleavage of Si-O-Si(Al) bonds in the GS glassy phase. This leads to the depolymerization of GS, generating oligomers such as [Al(OH)₄]⁻ and [SiO(OH)₃]⁻ complexes (Reactions (2) and (3))⁴⁰. These complexes gradually diffuse from the surface of GS into the solution, further react with Mg²⁺, Ca²⁺ and OH⁻ ions, leading to the formation of hydrotalcite (HT) and different forms of C-S-H gel, such as fibrous, flocculent, and honeycomb structures (Reaction (4)~(5)). In addition, the free Al³⁺ ions generated from the dissolution of the amorphous glass phase and C₂AS in GS enter the C-S-H and form C-A-S-H (Reaction (6)), resulting in an increase in total pore volume⁴¹. Due to the presence of SO₃ and Al₂O₃ in both GS and CS, some SO₄²⁻ ions are generated during the hydration process. In a high Ca²⁺ concentration and alkaline environment, petal-like AFm crystals are formed (Reaction (7)). Furthermore, the free CH in the pore water can absorb CO₂ from the air and water, leading to carbonate reactions that produce insoluble CaCO₃ precipitates (Reaction (8)). When the concentration of OH⁻ is high in GCCM, CH preferentially precipitates (as confirmed by SEM, in-situ FTIR and XRD analysis) (Reaction (9)).

Analysis of mechanical properties of GCCM and GBC

UCS analysis of GCCM and GBC

Figure 15 illustrates the compressive strength of GCCM. The results indicate that the compressive strength of GCCM with same mix ratio increases with the growth of curing age, showing significant changes in strength values at different ages. Specifically, the compressive strength values at 7 days compared to those at 3 days exhibited increases of 87.1, 87.5, 71.2, 117.3, and 98.9%, respectively. Furthermore, the strength values at 28 days, when compared to those at 14 days, showed increases of 17.7, 42.5, 46.9, 15.9, and 11.5%, separately. This indicates that the hydration reaction of GS and CS is relatively rapid within the first 7 days. As the curing time extends, the hydration products gradually adhere to the surface of the GS, forming a coating that impedes further hydration reactions of the GS, resulting in a gradual decrease in reaction rate and a reduction in the increment of compressive strength. Under different mix ratios, the strength values of GCCM at various ages exhibit a trend of initially increasing and then decreasing as the $n(\text{CaO})/n(\text{SiO}_2 + \text{Al}_2\text{O}_3)$ ratio increases, with

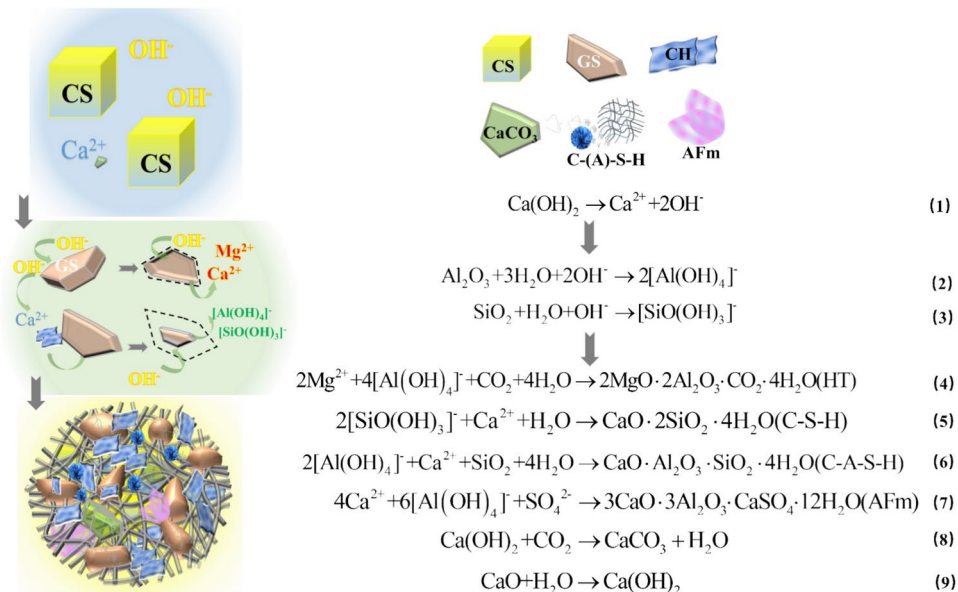


Fig. 14. Mechanism diagram of synergistic hydration of GCCM.

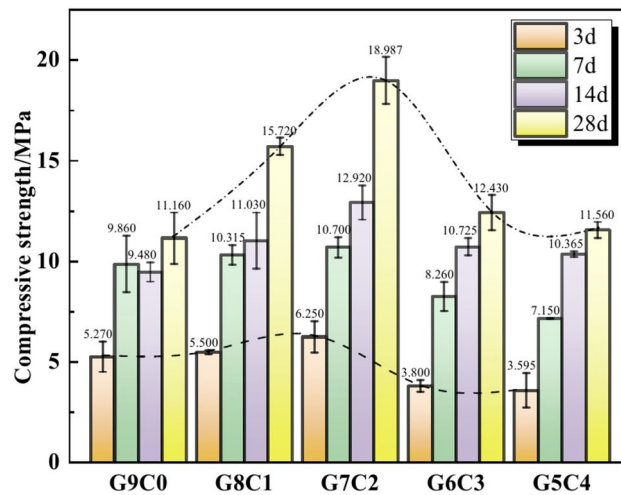


Fig. 15. Compressive strength of GCCM.

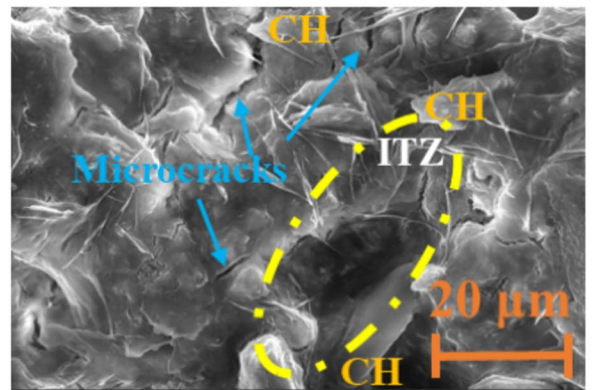
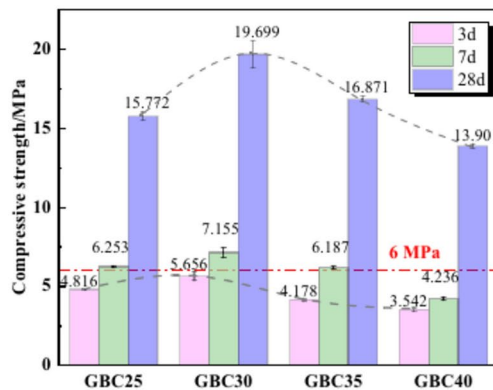


Fig. 16. Compressive strength of GBC. (S) Interface morphology of GBC35.

this trend being most pronounced at 28 days. This is attributed to the increased amount of main hydration products such as C-(A)-S-H and AFm, which enhance the density of the GCCM. While neither CaCO_3 nor CH directly contributes to strength, the ongoing hydration reactions increase the content of hydration products on the surfaces and around the GS and CS particles, reducing the distance between particles. The repulsive forces between particles are gradually overcome by van der Waals forces, leading to interlocking and agglomeration of crystals and hydration products, which fill the voids and pores between the sample particles. This phenomenon increases the roughness of GCCM surface and enhances the specific surface area (as confirmed by BET analysis), thereby improving the mechanical properties and micro-densities of GCCM^{18,42}. However, in systems with a high $n(\text{CaO})/n(\text{SiO}_2 + \text{Al}_2\text{O}_3)$ ratio, the lack of silica-alumina phases that consume CH results in an increased quantity of CH precipitating as a monolayer structure. This inhibits further dissolution and transport of Ca^{2+} and OH^- ions, with CH adhering to the surfaces of GS particles obstructing the dissolution of the reactive silica-alumina components, leading to a reduction in the quantity of primary hydration products like C-(A)-S-H (as evidenced by SEM, XRD and TG analysis), ultimately resulting in a decrease in the strength of the matrix.

Based on the UCS results for GCCM at 28d presented in Fig. 9, the optimum ratio of G7C2 was selected as the cementitious material for the GBC. As shown in Fig. 16, the compressive strength of the GBC at 28d exhibits a “anti-hook” trend, initially increasing and then decreasing with the increasing GCCM content. This observation is consistent with the findings reported by Fan⁴³ and Wu et al.⁴⁴. The GBC achieves its maximum compressive strength values at 3 days and 28 days, reaching 5.656 MPa and 19.699 MPa, respectively, which meets the 6 MPa UCS requirement for most coal mines⁴⁵. These values are also higher than those of conventional OPC backfill materials⁴⁶, and the ratio can be adjusted according to practical needs. The increase in GCCM content from 25wt.% to 30wt.% results in the generation of more hydration products such as C-(A)-S-H gel and AFm, facilitating the filling of voids between aggregates. This enhances the consolidation capability of the aggregates, leading to a denser microstructure that improves the compressive strength of the GBC. However, when the GCCM content exceeds 30wt.%, on the one hand, the proportion of aggregates decreases. The aggregates have a rigid framework role in the filling body, which fails to provide effective support, diminishes effective force transfer and negatively impacts the strength of the GBC. On the other hand, some microcracks were observed in

the micro-interface of the GBC35 sample (as shown in Fig. 16S). It is found that there are flaky CH crystals tends to accumulate at the boundaries of the aggregates. These crystals interact weakly with the aggregates primarily via van der Waals forces or hydrogen bonding, which facilitates the initiation of cracks at the aggregate interfaces⁴⁷. This indicates that the interface bonding between the aggregate and the GCCM matrix is not ideal in GBC35.

Analysis of stress–strain curve characteristics

To analyze the brittle–ductile failure mode of GCCM, the stress–strain curves of representative GCCM at 28d are plotted in Fig. 17A–E. The stress–strain curve of the GCCM can be divided into five distinct stages: a concave curve (I: densification stage), a inclined line (II: linear elastic stage), a convex fluctuating curve (III: plastic deformation stage), a concave curve (IV: post-peak failure instability stage), and a descending curve (V: post-peak residual load-carrying stage).

The stress–strain curves of GBC under uniaxial compression with varying GCCM contents are shown in Fig. 17F. The loading process can be divided into four stages: the initial densification stage (OA segment), the elastic compression stage (AB segment), the plastic failure stage (BC segment), and the post-peak failure stage (CD segment). It is observed that during the post-peak failure instability stage, as the GCCM content increases, the rate of decrease in stress after reaching the peak value accelerates, indicating a more pronounced brittle characteristic of the GBC⁴⁸. This phenomenon occurs possibly because the increase in GCCM alters the internal pore structure and defect distribution within the GBC, making it easier for microcracks and voids to form stress concentration zones, which accelerates crack propagation and material failure.

Analysis of elastic modulus

The strength of the samples is evaluated using the elastic modulus, defined as the slope of the rising segment of the stress–strain curve, which reflects the stiffness characteristics during the elastic phase. The variation curves of the elastic modulus for both GCCM and GBC are shown in Fig. 18A,B, respectively, and their trends follow a polynomial function characterized by exponential decay. According to the fitting results, as the CS content increases, the elastic modulus of GCCM initially increases significantly before gradually decreasing, which is consistent with the trend in compressive strength. When the ratio of $n(\text{CaO})/n(\text{SiO}_2 + \text{Al}_2\text{O}_3)$ in GCCM increases from 0.388 to 0.635, the elastic modulus of GCCM increases by 205.88%. The proper increase in CS leads to a higher amount of hydration products, which contributes to fill the pores and cracks within the GCCM, reducing internal defects and optimizing its microstructure. Consequently, GCCM can better resist deformation under stress, significantly enhancing its elastic modulus. However, when the ratio of $n(\text{CaO})/n(\text{SiO}_2 + \text{Al}_2\text{O}_3)$ exceeds 0.635, CH preferentially precipitates in a high OH^- environment, resulting in a decrease in the proportion of C-(A)-S-H and a corresponding decline in the overall strength of GCCM.

The elastic modulus of GBC exhibits a trend of first increasing and then decreasing with the increase in GCCM content. At a GCCM content of 30wt.%, the elastic modulus reaches its maximum value of 3.3GPa, which

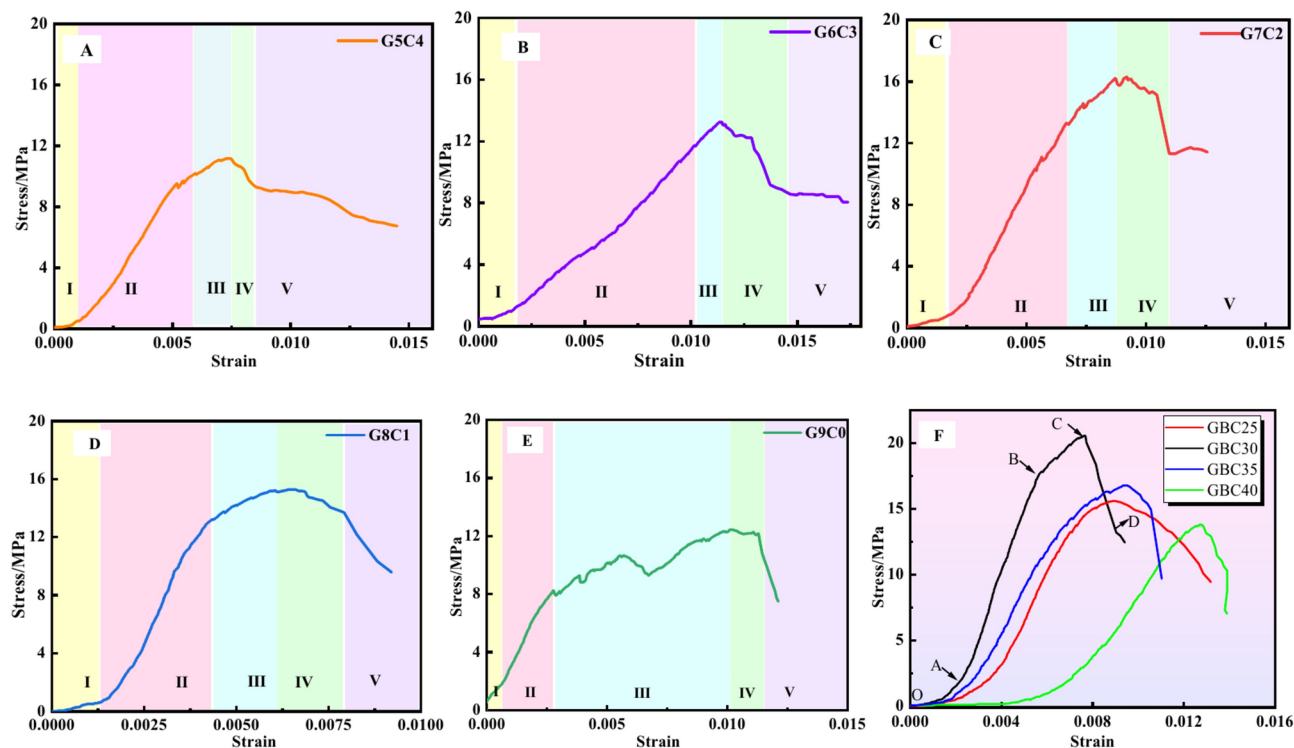


Fig. 17. Stress–strain curves of GCCM and GBC specimens. (A) G5C4; (B) G6C3; (C) G7C2; (D) G8C1; (E) G9C0; (F) GBC).

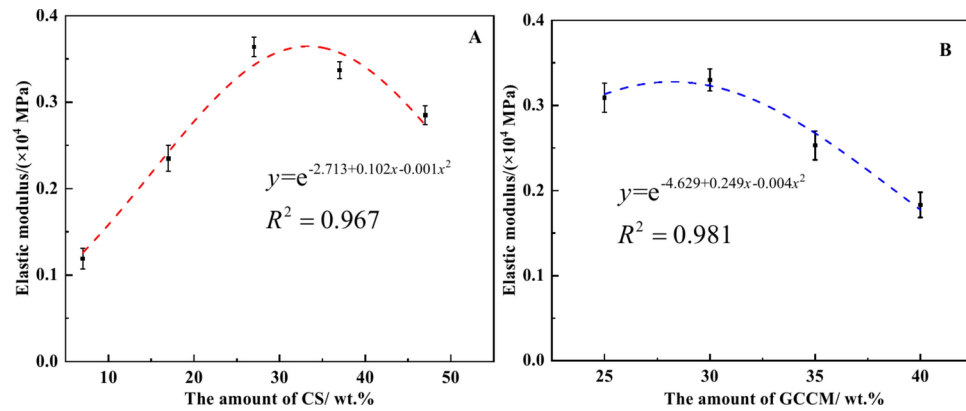


Fig. 18. Elastic modulus curves of GCCM and GBC. (A) GCCM; (B) GBC.

is significantly higher than that of filling body specimens with 5wt.% cement content⁴⁹, and it also demonstrates a quicker transition into the elastic phase⁵⁰. The hydration of GCCM generates C-(A)-S-H gel products, which possess cementing properties, enhancing the bond strength between aggregates and improving the interface bonding, thereby strengthening the overall structure of the GBC and increasing the elastic modulus. However, when the GCCM content exceeds 30wt%, a large amount of GCCM reduces the relative amount of aggregates, weakening the overall skeletal strength of the backfill body. In addition, the hydration products of GCCM tend to form new voids or cracks around the aggregates, weakening the interface bonding and impairing stress transfer.

Failure mechanism analysis

To investigate the failure modes of GCCM and GCB, a comparative analysis was conducted based on the content of CS, GCCM proportion, and curing age. Observations from Fig. 19 reveal that under axial loading, GCCM begins to exhibit micro-cracks at the ends, which gradually develop into long cracks that extend the height of the specimen over time. Two nearly parallel main cracks are formed on the left and right sides of the specimen, accompanied by a network of layered micro-cracks in the surrounding area. A bulging phenomenon resembling an “H” shape with a thickness of approximately 3 mm is observed on the surface of the specimen. As both longitudinal and lateral deformations increase, spalling occurs in the form of thin plates, all of which are results of stress concentration and crack propagation. The failure modes of GCCM can be categorized as follows: X-shaped conjugate shear failure, single-shear plane failure, and splitting failure⁵¹. The varying proportions of GS contribute to the complexity of the internal microstructure of GCCM, resulting in uneven stress distribution that influences the failure modes.

During uniaxial compression, the GBC exhibits certain longitudinal and transverse deformations. A main crack, close to the height of the specimen, appears on the surface, accompanied by multiple short cracks. However, compared to GCCM, the number of visible cracks is fewer, and their widths are smaller. It is observed that as the GCCM content increases, the visible damage to the 3d GBC specimen intensifies, and the degree of diagonal shear failure in the 28d GBC specimen also increases, predominantly characterized by splitting and tensile failure⁵¹. At 3d curing age, the hydration reaction is not yet complete, leading to insufficient gel network strength and weak bonding between the aggregates and the cementitious material interface, making the material more prone to failure under stress. The hydration of GCCM progresses sufficiently at 28d, enhancing the gel network and improving the bonding effect between the GCCM matrix and the aggregates. Additionally, the further propagation and connection of internal micro-cracks lead to the gradual spalling of the ends of the GBC, resulting in an increase in the area of the pits and a corresponding rise in the degree of damage.

Morphology analysis of GBC

Figure 20 shows the morphology of GBC. Prior to crushing, GBC exhibits a uniform and dense block structure with a slightly rough surface, predominantly gray in color. After conducting mechanical tests on GBC samples at 28d, a morphological analysis reveals that the shape is irregular with sharp edges, exposing the internal GBC, GS particles and the GCCM matrix structure. Various forms of damage were observed, including CG splitting failure, GCCM matrix fracture, and interface failure between the aggregate and the GCCM matrix, resulting in an internal structure resembling a “dense suspension”^{52,53}. Once the slurry solidifies, a small number of unreleased air bubbles create cavities within the material. The CG itself is internally loose and porous, which contributes to the notable porosity of GBC.

Further microscopic analysis of the GBC30 at 28d using SEM shows a dense transition zone at the interface between the GCCM and the aggregates, indicating strong bonding without any significant pores or micro-cracks. EDS results in Fig. 20 reveals the presence of numerous hydration products such as honeycomb-like, three-dimensional network, and fibrous C-(A)-S-H gel at the bonding interface. These products fill the gaps between the aggregate particles, forming a compact cementitious structure. From a microstructural perspective, the dense cementitious matrix and the strong interfacial bonding between the aggregates and the matrix align with the higher mechanical strength test results observed for GBC30.

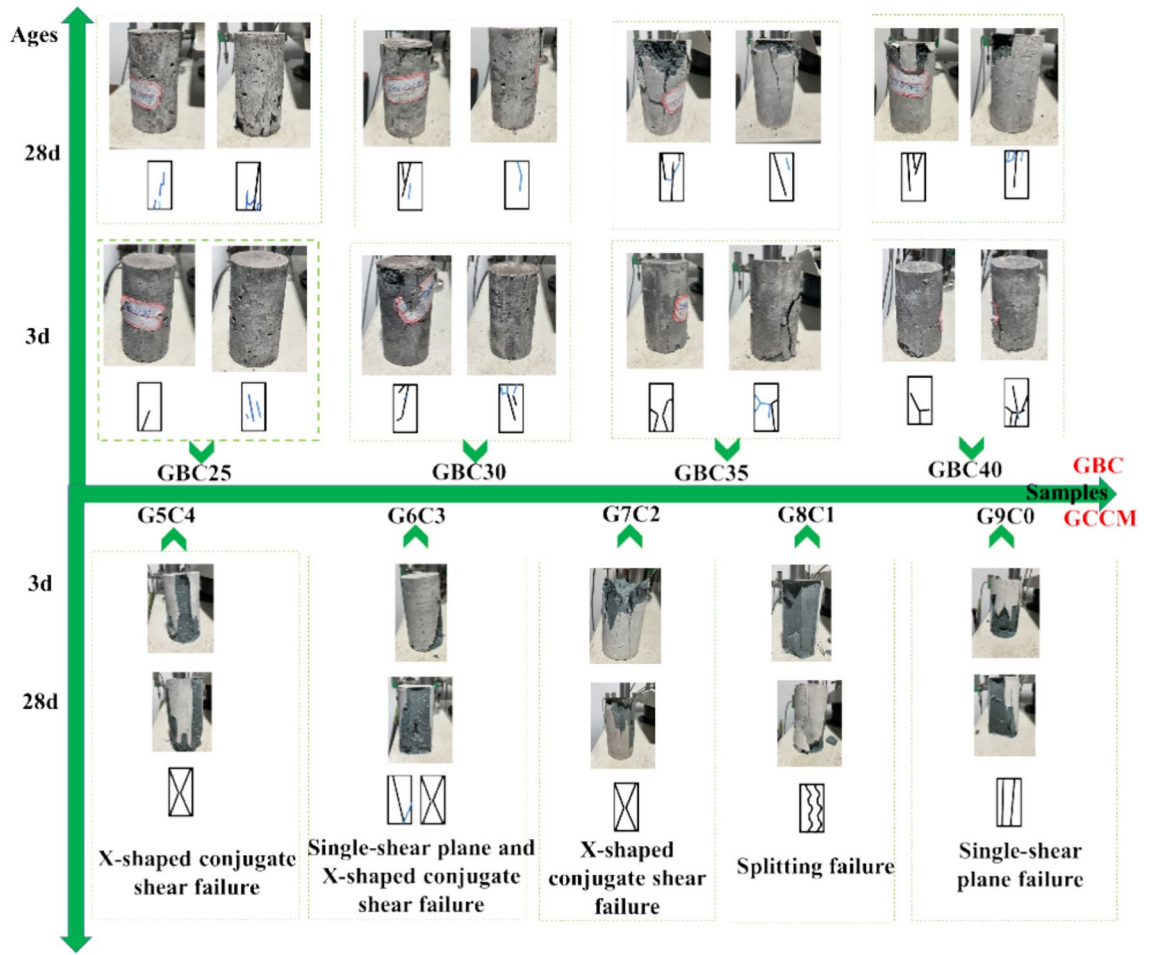


Fig. 19. Failure mechanism analysis of GBC and GCCM.

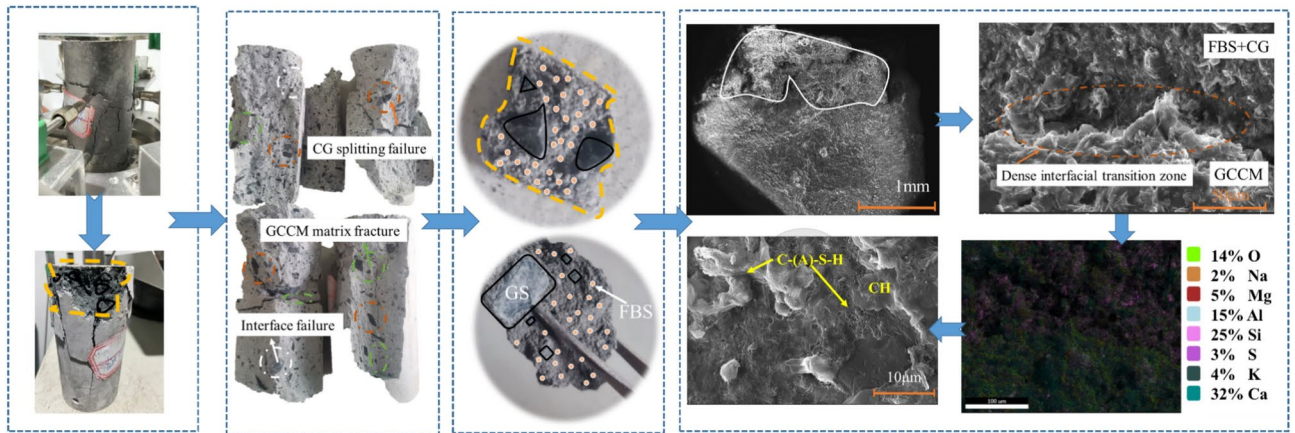


Fig. 20. Morphology of GBC.

Working performance of GCCM and GBC

Flowability and water bleeding rate of GCCM

The test results shown in Fig. 21 indicate that the flowability and water bleeding rate of the GCCM slurry samples significantly decrease with an increase in $n(\text{CaO})/n(\text{SiO}_2 + \text{Al}_2\text{O}_3)$, and the color of the slurry transitions from medium gray to gray-white. On one hand, the cumulative volume of CS at 10 μm is greater than that of GS (as shown in Fig. 5), and its specific surface area is also higher than that of GS, which has a higher water absorption capacity. This results in a reduction in the free water content in the slurry, alleviating the bleeding phenomenon.

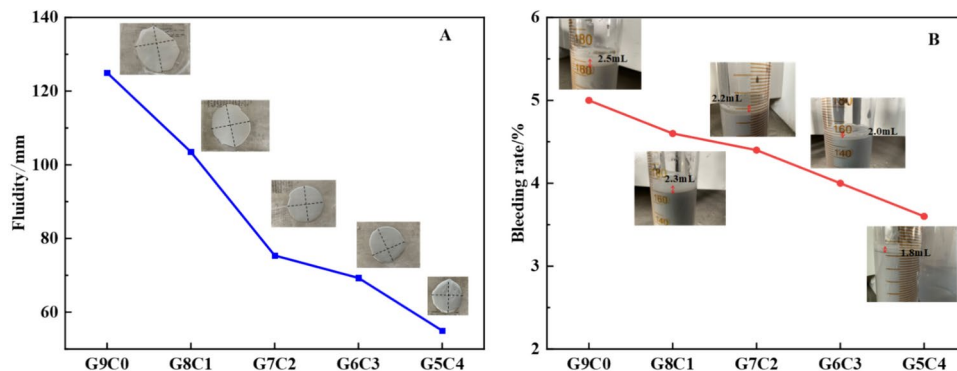


Fig. 21. The fluidity and bleeding rate of GCCM. (A) fluidity; (B) bleeding rate.

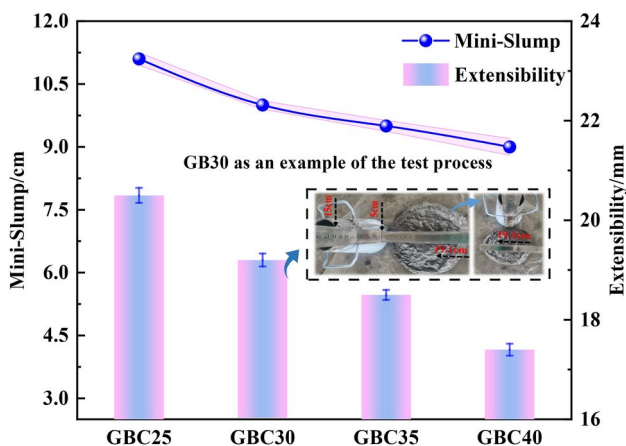


Fig. 22. Change in mini-slump and extensibility of GBC.

It also weakens the lubricating effect between particles, making it more difficult for solid particles to slide against each other during shear, thus increasing the viscosity of the slurry and reducing its flowability⁵⁴. On the other hand, as the $n(\text{CaO})/n(\text{SiO}_2 + \text{Al}_2\text{O}_3)$ molar ratio increases, the incorporation of CS progressively rises, the dissolution of CH in water generates an exothermic reaction that consumes water in the system and effectively bounds a greater amount of free water, thereby reducing both its liquidity and water bleeding rate.

The fluidity of GBC

The slump test is a crucial indicator of the cohesion and frictional resistance of slurry materials. Following the guidelines of GB/T 50,080, a micro slump test apparatus was utilized to measure the mini-slump value of GBC 30 freshly mixed grout. The test results in Fig. 22 indicate that the mini-slump and extensibility of GBC decrease as the GCCM content increases. This is primarily due to the significantly smaller particle size of the GCCM compared to CG and FBS, which have a higher specific surface area. As a result, GCCM absorbs more water, increasing the internal friction within the slurry, leading to a reduction in both slump and extensibility^{55,56}. Research indicates that backfill materials with a mini-slump greater than 7.1 cm are considered to possess good transportability²¹. Therefore, GBC exhibits excellent fluidity, allowing for effective pipeline transportation.

Environmental impact and cost analysis of GBC

Leachability of heavy metals in GBC

As summarized in Table 7, detectable concentrations of heavy metals such as Hg, Cr, and Pb were found in both the GBC samples and their raw materials. However, all measured values fall within the maximum allowable discharge limits for heavy metals as specified in GB 8978, “Comprehensive Discharge Standards for Wastewater”. A comparison with the raw materials reveals that the concentrations of Hg and Pb in the cured GBC samples are both lower than those in the raw materials. The target element Cr was found at concentrations of 0.0206 and 0.0275 mg/L in GBC30 and GBC40, respectively, both of which are below the maximum content levels for CG. This indicates that GBC has a good capacity for heavy metal immobilization, attributed to the rich presence of C-(A)-S-H gel and other hydration products that facilitate heavy metal solidification. These findings are consistent with the research results of Yang et al.²¹.

Elements	Raw material and GBC samples								Standards limits	Unit
	CG	FBS	GS	CS	GBC25	GBC30	GBC35	GBC40	GB 8978	
Hg	4.7085	3.1050	5.4334	3.8256	2.7674	2.6662	2.8934	2.8373	50	µg/L
Cr	0.0384	0.0194	0.0212	0.0222	0.0243	0.0206	0.0254	0.0275	1.5	mg/L
Pb	0.0116	0.0038	0.0056	0.0055	0.0038	0.0034	0.0041	0.0039	1.0	mg/L

Table 7. Heavy metal leaching results of raw materials and GBC samples.

Raw materials	CG	FBS	CS	GS	Mixing water	OPC
Type	Solid waste/ By-product	Solid waste/ By-product	Solid waste/ By-product	Product	Tap water	Product
GWP (kg CO ₂ -eq/kg)	–	3.12×10^{-2}	6.70×10^{-2}	1.69×10^{-2}	1.55×10^{-4}	0.92
Cost (RMB/kg)	0.10	0.10	0.15	0.17	6.40×10^{-3}	0.40

Table 8. GWP and cost analysis of GBC raw materials.

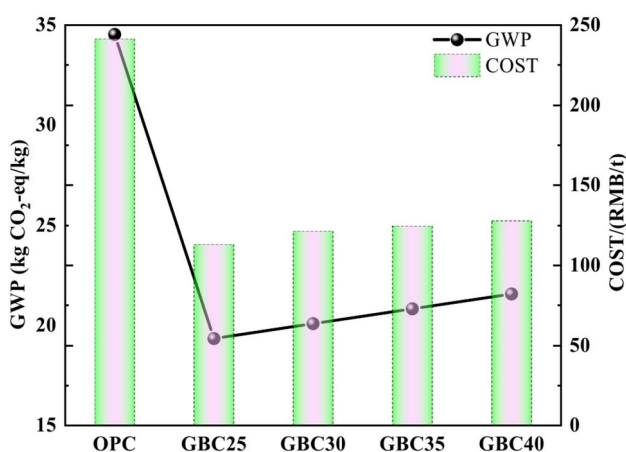


Fig. 23. GWP and cost of OPC and GBC for 1 t mixture.

GWP and cost analysis of GBC

A lifecycle assessment (LCA) was conducted to compare the global warming potential (GWP) and costs of the fully solid waste GBC backfill material with those of OPC-based backfill materials, as presented in Table 8. The emission data for various raw material impact factors were referenced from GB/T 51,366, the China Life Cycle Data Center (CLCD), relevant literature^{57,58}, and the Ecoinvent 3.8 database⁵⁹. In this analysis, only the highest transportation costs for CG and FBS were considered, while the impact of CG on the comprehensive cost index and implicit CO₂ index was omitted due to its carbon emissions primarily resulting from self-ignition during storage⁶⁰. Additionally, energy consumption and associated carbon emissions from CS during drying and grinding are inevitable. Calculating with an electricity cost of 0.5RMB/kWh and a carbon emission factor of 0.785 kg/kWh⁶¹, the energy consumption and carbon emissions were determined to be 18 kWh/t and 0.014 kg/kWh, respectively. The final calculations depicted in Fig. 23 demonstrate that, taking GBC30 sample as an example, compared to OPC backfill materials, the global warming potential and cost of 1 ton of GBC were reduced by 41.27 and 50.14%, separately. It is particularly emphasized that the carbon emissions from CS are difficult to quantify; thus, the study references the calculations for quicklime in industrial production⁶¹. Therefore, the actual carbon emissions from GBC are likely to be even lower. Furthermore, the utilization rate of the OPC filling material in this assessment was assumed to be 75%⁴⁰, while GBC achieved a 100% utilization of full-solid waste. In conclusion, GBC serves as an environmentally friendly mining backfill material that effectively reduces costs, decreases carbon emissions, and enhances solid waste utilization efficiency.

Conclusion

The synergistic hydration mechanism of preparing GCCM using industrial solid waste GS and alkaline solid waste CS has been revealed, and the practicality of GCCM cementing FBS and CG as underground mine backfill materials has been explored. The conclusions are as follows:

- (1) A significant synergistic effect exists between GS and CS. Under the activation of CS, reactive minerals in CS dissolve, and generating hydration products primarily composed of C-(A)-S-H gel, AFm phase and hydrotalcite, which are crucial for the improved strength of GCCM.

(2) When the molar ratio of $n(\text{CaO})/n(\text{SiO}_2 + \text{Al}_2\text{O}_3)$ is 0.635, the UCS of GCCM and GBC at 28d are 18.987 and 19.699 MPa, respectively. Both GCCM and GBC display typical elastic–plastic characteristics in their stress–strain curves. Under compression, GBC exhibits tensile failure and oblique shear failure, accompanied by end spalling. The fracture surface exhibits damage patterns including aggregate fracture, GCCM matrix fracture, and fracture at the aggregate–GCCM matrix interface.

(3) The developed GCCM offers eco-friendly, low-carbon alternatives to traditional cement and holds significant potential in the mining industry, as well as in structural concrete, road construction, and other civil engineering projects. The incorporation of FBS and CG into GCCM enhances its effectiveness as mine backfill GBC, supporting sustainable mining practices and reducing the environmental impact of mining activities.

(4) The strength, fluidity and leaching of GBC meets the filling strength, transportation and environmental requirements for mining applications. Compared to OPC-based backfill materials, GBC offers economic, and carbon reduction advantages.

Future research should explore the effects of varying additive amounts and curing conditions on the performance of GCCM and GBC, as well as long-term performance assessments, including durability and microstructural evolution, to optimize formulation design and broaden its application scope.

Data availability

The datasets used and analyzed during the current study available from the corresponding author on reasonable request.

Received: 21 October 2024; Accepted: 10 January 2025

Published online: 14 January 2025

References

- National Energy Group Technical and economic Research Institute. *Annual Report on Coal Industry in China* (China Coal Industry Association, 2023).
- Wang, Y., Abbas, T. & Xu, X. Application of coal mine roof rating in Chinese coal mines. *Int. J. Min. Sci. Technol.* **28**(03), 491–497. <https://doi.org/10.1016/j.ijmst.2018.04.005> (2018).
- Zhang, J. X. et al. Properties and application of backfill materials in coal mines in China. *Minerals* **9**(01), 53. <https://doi.org/10.3390/min9010053> (2019).
- Yang, K. et al. Theory and technology of solid waste underground green filling mining in coal power base of Yellow River Basin. *J. China Coal Soc.* **46**(S2), 925–935. <https://doi.org/10.13225/j.cnki.jccs.st21.0284> (2021).
- Yilmaz, T. et al. Assessment of strength properties of cemented paste backfill by ultrasonic pulse velocity test. *Ultrasonics* **54**(05), 1386–1394. <https://doi.org/10.1016/j.ultras.2014.02.012> (2014).
- Yang, G. H. et al. Effect of carbide slag and steel slag as alkali activators on the key properties of carbide slag–steel slag–phosphogypsum composite cementitious materials. *Front. Mat.* <https://doi.org/10.3389/fmats.2024.1353004> (2024).
- Liu, Y. T. et al. Recycling phosphogypsum in subbase of pavement: Treatment, testing, and application. *Constr. Build. Mater.* **342**, 127948. <https://doi.org/10.1016/j.conbuildmat.2022.127948> (2022).
- Zhu, C. F. et al. Enhancement of ultra-fine slag on compressive strength of solid waste-based cementitious materials: Towards low carbon emissions. *J. Build. Eng.* **63**, 105475. <https://doi.org/10.1016/j.job.2022.105475> (2023).
- Zhou, L. B. et al. Hydration hardening characteristics of steel slag–red mud–cement based composite mortar. *Bull. Chin. Ceram. Soc.* **42**(08), 2837–2845. <https://doi.org/10.16552/j.cnki.issn1001-1625.20230614.002> (2023).
- Garcia-Lodeiro, I. et al. Alkaline activation of synthetic aluminosilicate glass. *Ceram. Int.* **40**(04), 5547–5558. <https://doi.org/10.1016/j.ceramint.2013.10.146> (2014).
- Hafez, H. et al. Assessing the sustainability potential of alkali-activated concrete from electric arc furnace slag using the ECO2 framework. *Constr. Build. Mater.* **281**, 122559. <https://doi.org/10.1016/j.conbuildmat.2021.122559> (2021).
- Yu Y. Research and development of new cemented filling materials for coal mines and their properties. Ph.D. China University of Mining and Technology (Beijing). CNKI: CDMD:1.1017.237817. (2017).
- Sun, R. Y. et al. CO₂ capture using carbide slag modified by propionic acid in calcium looping process for hydrogen production. *Int. J. Hydrogen Energy* **38**(31), 13655–13663. <https://doi.org/10.1016/j.ijhydene.2013.08.030> (2013).
- Ma, Z. H., Liao, H. Q. & Cheng, F. Q. Synergistic mechanisms of steelmaking slag coupled with carbide slag for CO₂ mineralization. *Int. J. Greenhouse Gas Control* **105**, 103229. <https://doi.org/10.1016/j.jggc.2020.103229> (2021).
- Guo, W. C. et al. Mechanical performance and microstructure improvement of soda residue–carbide slag–ground granulated blast furnace slag binder by optimizing its preparation process and curing method. *Constr. Build. Mater.* **302**, 124403. <https://doi.org/10.1016/j.conbuildmat.2021.124403> (2021).
- Bai, Y. Y. et al. Strength formation mechanism and curing system optimization of low-carbon cementitious materials prepared by synergistic activation of multiple alkaline solid wastes. *Constr. Build. Mater.* **402**, 132931. <https://doi.org/10.1016/j.conbuildmat.2023.132931> (2023).
- Chen, R. Y. et al. Study on the effect of slag content on the mechanical properties of filling body. *Min. Res. Dev.* **42**(03), 71–75. <https://doi.org/10.13827/j.cnki.kyyk.2022.03.004> (2022).
- Chen, D. H. et al. Study on optimization of less hydration ratio of bulk coal-based solid waste paste filling material. *Min. Saf. Environ. Protect.* **51**(04), 146–155. <https://doi.org/10.19835/j.issn.1008-4495.20240131> (2024).
- Li, B. L. Hydration mechanism and durability of cement–nickel slag–lithium slag binary and ternary composite cementitious materials. *Southeast Univ.* <https://doi.org/10.27014/d.cnki.gdnau.2019.004063> (2019).
- Li, W. T. & Yi, Y. L. Use of carbide slag from acetylene industry for activation of ground granulated blast-furnace slag. *Constr. Build. Mater.* **238**, 117713. <https://doi.org/10.1016/j.conbuildmat.2019.117713> (2020).
- Yang, P. et al. Investigating the synergistic effects of magnesia–coal slag based solid waste cementitious materials and its basic characteristics as a backfill material. *Sci. Total Environ.* **880**, 163209. <https://doi.org/10.1016/j.scitotenv.2023.163209> (2023).
- Lu, H. Y. Study on mechanical properties and damage constitutive model of loess–slag–based cemented filling materials. *China Univ. Min. Technol.* <https://doi.org/10.27623/d.cnki.gzkyu.2023.002464> (2023).
- Tang, R. et al. Experimental study on the effect of fly ash with ammonium salt content on the properties of cemented paste backfill. *Constr. Build. Mater.* **369**, 130513. <https://doi.org/10.1016/j.conbuildmat.2023.130513> (2023).
- Ruan, S. et al. Application of desulfurization gypsum as activator for modified magnesium slag–fly ash cemented paste backfill material. *Sci. Total Environ.* **869**, 161631. <https://doi.org/10.1016/j.scitotenv.2023.161631> (2023).
- Zhang, J. et al. Utilization of carbide slag–granulated blast furnace slag system by wet grinding as low carbon cementitious materials. *Constr. Build. Mater.* **249**, 118763. <https://doi.org/10.1016/j.conbuildmat.2020.118763> (2020).

26. Kapeluszna, E. et al. Incorporation of Al in C-A-S-H gels with various Ca/Si and Al/Si ratio: Microstructural and structural characteristics with DTA/TG, XRD, FTIR and TEM analysis. *Constr. Build. Mater.* **155**, 643–653. <https://doi.org/10.1016/j.conbuildmat.2017.08.091> (2017).
27. Myers, R. J. et al. Thermodynamic modelling of alkali-activated slag cements. *Appl. Geochem.* **61**, 233–247. <https://doi.org/10.1016/j.apgeochem.2015.06.006> (2015).
28. Salihi, M. A. et al. Effect of different curing temperatures on alkali activated palm oil fuel ash paste. *Constr. Build. Mater.* **94**, 116–125. <https://doi.org/10.1016/j.conbuildmat.2015.06.052> (2015).
29. Wang, G. J. et al. Mechanical properties and microscopic characterization of cemented paste backfill with electrolytic manganese residue matrix binder. *J. Mater. Res. Technol.* **23**, 2075–2088. <https://doi.org/10.1016/j.jmrt.2023.01.098> (2023).
30. Shen, S. et al. Explore the synergic and coupling relationships of multiple industrial solid wastes in the preparation of alkali-activated materials under different curing regimes. *Mater. Today Sustain.* **19**, 100169. <https://doi.org/10.1016/j.mtsust.2022.100169> (2022).
31. Dou, H. Y. Preparation and characterization of geopolymer-based lithium molecular sieves. *Guangxi Univ.* <https://doi.org/10.27034/d.cnki.ggxui.2023.002271> (2023).
32. Xu, B. & Yi, Y. Use of ladle furnace slag containing heavy metals as a binding material in civil engineering. *Sci Total Environ.* **705**, 135854. <https://doi.org/10.1016/j.scitotenv.2019.135854> (2020).
33. Maria, C. & Garci, J. Examining the relationship between the microstructure of calcium silicate hydrate and drying shrinkage of cement pastes. *Cement Concr. Res.* **32**, 289–296. [https://doi.org/10.1016/S0008-8846\(01\)00673-1](https://doi.org/10.1016/S0008-8846(01)00673-1) (2002).
34. Li, N., Farzadnia, N. & Shi, C. Microstructural changes in alkali-activated slag mortars induced by accelerated carbonation. *Cement Concr. Res.* <https://doi.org/10.1016/j.cemconres.2017.07.008> (2017).
35. Puertas, F. et al. A model for the C-A-S-H gel formed in alkali-activated slag cements. *J. Eur. Ceram. Soc.* **31**(12), 2043–2056. <https://doi.org/10.1016/j.jeurceramsoc.2011.04.036> (2011).
36. Wan, Z. H. et al. Study on properties of carbide slag-slag composite cementitious material. *Bull. Chin. Sil.* **41**(05), 1704–1714. <https://doi.org/10.16552/j.cnki.issn1001-1625.2022.05.015> (2022).
37. Li, Y., Qiao, C. & Ni, W. Green concrete with ground granulated blast-furnace slag activated by desulfurization gypsum and electric arc furnace reducing slag. *J. Clean. Prod.* **269**, 122212. <https://doi.org/10.1016/j.jclepro.2020.122212> (2020).
38. Ruan, S. S. et al. Development and field application of a modified magnesium slag-based mine filling cementitious material. *J. Cleaner Prod.* **419**, 138269. <https://doi.org/10.1016/j.jclepro.2023.138269> (2023).
39. El-Jazairi, B. & Illston, J. M. The hydration of cement paste using the semi-isothermal method of derivative thermogravimetry. *Cement Concr. Res.* **10**(30), 361–366. [https://doi.org/10.1016/0008-8846\(80\)90111-8](https://doi.org/10.1016/0008-8846(80)90111-8) (1980).
40. Li, K. X. et al. Innovative synthesis of low-carbon cemented backfill materials through synergistic activation of solid wastes: An integrated assessment of economic and environmental impacts. *Case Stud. Constr. Mater.* **20**, e03203. <https://doi.org/10.1016/j.cscm.2024.e03203> (2024).
41. Mohamed, O. A. Effect of immersing geopolymer slag-fly ash mortar in sulfuric acid on strength development and stability of mass. *Constr. Build. Mater.* **341**, 127786. <https://doi.org/10.1016/j.conbuildmat.2022.127786> (2022).
42. Zhu, X. et al. Effect of calcium carbide residue on strength development along with mechanisms of cement-stabilized dredged sludge. *Materials* **15**(13), 4453. <https://doi.org/10.3390/ma15134453> (2022).
43. Fan, D. L. Compressive performance and microscopic characterization of solid waste matrix coal gangue concrete. *Clean Coal Technol.* **30**(S2), 216–222. <https://doi.org/10.13226/j.issn.1006-6772.23112803> (2024).
44. Wu, C. L. et al. A sustainable low-carbon pervious concrete using modified coal gangue aggregates based on ITZ enhancement. *J. Cleaner Prod.* **377**, 134310. <https://doi.org/10.1016/j.jclepro.2022.134310> (2022).
45. Zhou, A. et al. A novel approach for recycling engineering sediment waste as sustainable supplementary cementitious materials. *Resour. Conserv. Recycl.* **167**, 105435. <https://doi.org/10.1016/j.resconrec.2021.105435> (2021).
46. Shi, X. L., Wang, X. L. & Wang, X. L. Dual waste utilization in cemented paste backfill using steel slag and mine tailings and the heavy metals immobilization effects. *Powder Technol.* **403**, 117413. <https://doi.org/10.1016/j.powtec.2022.117413> (2022).
47. Huang, L. et al. Composition and microstructure of 50-year lightweight aggregate concrete (LWAC) from nanjing yangtze river bridge (NYRB). *Constr. Build. Mater.* **216**, 390–404. <https://doi.org/10.1016/j.conbuildmat.2019.05.015> (2019).
48. Feng, G. R. et al. Study on damage evolution and failure characteristics of backfill column under uniaxial compression. *J. Cent. South Univ. (Sci. Technol.)* **53**(10), 4012–4023 (2022).
49. Wang, Y. Y., Yu, Z. Q. & Cui, L. Z. Uniaxial compression test of paste filling materials with different water content. *Coal Sci. Technol.* **50**(06), 219–224. <https://doi.org/10.13199/j.cnki.cst.2020-0251> (2022).
50. Zhao, Y. H. et al. 2022 Study on damage evolution and failure characteristics of cemented gangue backfill with different aspect ratios under uniaxial compression. *J. Min. Saf. Eng.* **39**(04), 674–682. <https://doi.org/10.13545/j.cnki.jmse.2021.0197> (2022).
51. Yang, K. et al. Experimental study on mechanics and deformation failure characteristics of multi-source coal-based solid waste cemented backfill. *Coal Geol. Explor.* **52**(06), 102–114. <https://doi.org/10.12363/issn.1001-1986.24.03.0188> (2024).
52. Mehdipour, I. & Khayat, H. K. Elucidating how particle packing controls rheology and strength development of dense cementitious suspensions. *Cement Concr. Compos.* **104**, 103413. <https://doi.org/10.1016/j.cemconcomp.2019.103413> (2019).
53. Wang, X. W. et al. The movement property characterization of coarse aggregate during gyratory compaction based on 3D-printed aggregate. *Constr. Build. Mater.* **361**, 129608. <https://doi.org/10.1016/j.conbuildmat.2022.129608> (2022).
54. Feng, Y. et al. Mechanical properties and microstructure of iron tailings cemented paste backfills using carbide slag-activated ground granulated blast-furnace slag as alternative binder. *Minerals* **12**(12), 1549. <https://doi.org/10.3390/min12121549> (2022).
55. Celik, F. & Canakci, H. An investigation of rheological properties of cement-based grout mixed with rice husk ash (RHA). *Constr. Build. Mater.* **91**, 187–194. <https://doi.org/10.1016/j.conbuildmat.2015.05.025> (2015).
56. Liu, L. et al. Co-disposal of magnesium slag and high-calcium fly ash as cementitious materials in backfill. *J. Clean. Prod.* **279**, 123684. <https://doi.org/10.1016/j.jclepro.2020.123684> (2021).
57. Guo, L. Z. et al. Mechanical properties and microstructure evolution of alkali-activated GGBS-fly ash-steel slag ternary cements. *Constr. Build. Mater.* **444**, 137727. <https://doi.org/10.1016/j.conbuildmat.2024.137727> (2024).
58. Zhang, W. W. et al. Effects of recycled carbon fibers on mechanical and piezoresistive properties and environmental impact in alkali-activated cementitious materials. *J. Clean. Prod.* **450**, 141902. <https://doi.org/10.1016/j.jclepro.2024.141902> (2024).
59. Ouellet, Plamondon C. & Habert, G. 25-life cycle assessment (LCA) of alkali-activated cements and concretes. In *Handbook of Alkali-Activated Cements, Mortars and Concretes* (eds Pacheco-Torgal, F. et al.) 663–686 (Woodhead Publishing, 2015).
60. Dou, G. L. et al. Preparation and characterization of green lignin modified mineral cementitious fireproofing materials based on uncalcined coal gangue and coal fly ash. *Constr. Build. Mater.* **435**, 136799. <https://doi.org/10.1016/j.conbuildmat.2024.136799> (2024).
61. Yang, J. et al. Sustainable clinker-free solid waste binder produced from wet-ground granulated blast-furnace slag, phosphogypsum and carbide slag. *Constr. Build. Mater.* **330**, 127218. <https://doi.org/10.1016/j.conbuildmat.2022.127218> (2022).

Acknowledgements

The authors gratefully acknowledge the financial support provided by the National Key Research and Development Program of China (No. 2018YFC0808100) and the Natural Science Foundation project of Hebei Province (E2024209057).

Author contributions

Li J.M.: Conceptualization, Methodology, Writing-original draft, Writing-review & editing. Guo L.W.: Investigation, Visualization, Funding acquisition, Writing-review & editing. Zhang J.Y.: Validation, Methodology, Formal analysis, Writing-review & editing, Funding acquisition. Li Y.: Methodology, Formal analysis, Writing-review & editing. Ma L.: Validation, Visualization. Wang K.: Investigation, Visualization.

Declarations

Competing interests

The authors declare no competing interests.

Additional information

Correspondence and requests for materials should be addressed to L.G. or J.Z.

Reprints and permissions information is available at www.nature.com/reprints.

Publisher's note Springer Nature remains neutral with regard to jurisdictional claims in published maps and institutional affiliations.

Open Access This article is licensed under a Creative Commons Attribution-NonCommercial-NoDerivatives 4.0 International License, which permits any non-commercial use, sharing, distribution and reproduction in any medium or format, as long as you give appropriate credit to the original author(s) and the source, provide a link to the Creative Commons licence, and indicate if you modified the licensed material. You do not have permission under this licence to share adapted material derived from this article or parts of it. The images or other third party material in this article are included in the article's Creative Commons licence, unless indicated otherwise in a credit line to the material. If material is not included in the article's Creative Commons licence and your intended use is not permitted by statutory regulation or exceeds the permitted use, you will need to obtain permission directly from the copyright holder. To view a copy of this licence, visit <http://creativecommons.org/licenses/by-nc-nd/4.0/>.

© The Author(s) 2025